Hemodynamics of Transition from Fetal-to-Neonatal Circulation: Modeling of Clinical Pre- and Perinatal Interventions

by

Mehmet Berk Yiğit

A Thesis Submitted to the
Graduate School of Sciences and Engineering
in Partial Fulfillment of the Requirements for
the Degree of

Master of Science
in
Bio-Medical Sciences and Engineering

Koç University

July 2014

Koç University

Graduate School of Sciences and Engineering

This is to certify that I have examined this copy of a master's thesis by

Mehmet Berk Yiğit

and have found that it is complete and satisfactory in all respects,
and that any and all revisions required by the final
examining committee have been made.

Committee Members:

_____

Kerem Pekkan, Ph. D. (Advisor)

_____

Metin Muradoğlu, Ph. D.

_____

Ahmet Şaşmazel, M. D., Ph. D.

Date: _____

ABSTRACT

Lumped parameter models (LPM) are used extensively for the investigation of the global adult and fetal circulatory blood flow physiology. A LPM is developed for the healthy fetal circulation at term. Two applications of the fetal LPM are the investigation of 1) the effect of umbilical cord clamping on the hemodynamics and gas exchange of the transition from fetal to neonatal circulation, 2) the impact of maternal hyperoxygenation on the arterial flow dynamics for the promotion of vascular growth in the hypoplastic left heart syndrome (HLHS) fetus.

Hemodynamics of fetal to neonatal transition is orchestrated through complex physiological changes and results in cardiovascular adaptation to adult biventricular circulation. Clinical practice during this critical period can influence vital organ physiology both for normal newborns and for patients with congenital heart defects. Particularly, the cord clamping procedure, immediate (ICC) vs. delayed cord clamping (DCC) is observed to be an important factor for the *transitory fetal hemodynamics*. The clinical need for a quantitative understanding of this physiology motivated the development of a LPM of the fetal cardio-respiratory system covering late-gestation to neonatal period.

In the first application, ICC and DCC procedures are investigated to elucidate their relative influence on the ventricular and respiratory performances during the transition to extrauterine circulation. LPM is validated and employed to predict the effects of cord clamping procedures on the hemodynamics and vital gases. We introduced clinical time-dependent resistance functions to simulate the vascular changes. For DCC, placental transfusion (53 ml) increased neonatal blood volume by 19.3%. This increased blood volume is reflected in an increase in preload pressures by 32% in left and by 73% in right ventricles compared to ICC , which in turn increased the cardiac output (CO) by 20% (CO_{ICC}= 1148 ml/min; CO_{DCC}=1379 ml/min). Our model accurately predicted dynamic flow patterns *in vivo*. DCC was shown to maintain oxygenation if the onset of pulmonary respiration is delayed or impaired. On the other hand, significant decrease by 20-25% in oxygen saturations was observed in the ICC under the same physiological conditions. We conclude that DCC has a significant impact on newborn hemodynamics, mainly because of the improved blood volume, and the sustained placental respiration.

The second application is devoted to the parametric investigation of the impact of pulmonary and ductus arteriosus (DA) vasomodeling under increased fetal oxygen tension on the steady and pulsatile flow dynamics in the aortic region of HLHS. LPM parameters are altered to model fetal HLHS circulation by decreasing the size of left ventricle and aortic vasculature. Vasoconstriction of the DA and vasodilatation in the pulmonary bed were modeled as an increase in the DA resistance (maximal increase by sixteen folds) and a decrease in the pulmonary vascular resistance (PVR) (maximal decrease by 75%). Vasoconstriction of ductus arteriosus and vasodilatation of pulmonary vasculature effectively improved the pulmonary venous return and the left ventricular output compared to baseline conditions. Pulsatile and mean flow rates in the ascending aorta and in the aortic arch increased by two folds under maximal hyperoxygenation conditions. Pulsatility index (PI) in the ascending aorta is consistent in all cases indicating that flow pulsatility changes proportionally with the mean aortic flow. PI in the DA decreases with increased DA resistance, and increased with decreased PVR.

Chapter 1 is devoted to the introduction to the cardiovascular physiology and LPM. Chapter 2, Chapter 3, and Chapter 4 provides necessary background for the theroretical and numerical aspects of the governing equations employed in the hemodynamic and respiratory LPM. In Chapter 5, LPM of the fetal circulation is constructed and validated with clinical data. In Chapter 6 and Chapter 7, applications of umbilical cord clamping and maternal hyperoxygenation therapy are presented.

ÖZET

Yetişkin ve fetal dolaşım sistemlerinde global kan akış fizyolojisinin incelenmesinde Lumped Parametre Modelleri (LPM) yaygın olarak kullanılır. Geç dönem fetal dolaşımı incelemek icin bir LPM geliştirildi. Fetal LPM iki klinik uygulamanın incelenmesinde kullanıldı: 1) umbilikal kordonun erken veya geç klemplenmesinin fetalden yenidoğan dolaşım sistemine geçişte kan akış dinamikleri ve solunum üstündeki etkileri, 2) hipoplastik sol kalp sendromu (HSKS) fetüslerinde maternal hiperoksijenasyon tedavisinin hipoplastik damarlardaki gelişmeyi desteklemesi açısından arteriyel akış dinamikleri üzerindeki etkisi.

Fetalden yenidoğan dolaşım sistemine geçişteki kan akış dinamikleri kompleks fizyolojik değişimler tarafından yönetilir ve bu süreç yetişkin biventriküler dolaşım sistemine adaptasyonla sonuçlanır. Bu kritik dönemdeki klinik uygulamaların sağlıklı yenidoğanlarda ve konjenital kalp bozuklularına sahip yenidoğan hastalarda organ fizyolojisi üstünde hayati etkileri vardır. Özellikle, erken ve geç umbilikal kordon klempleme prosedürlerinin *geçişsel (fetalden yenidoğana) kan akış dinamikleri*nde önemli bir faktör olduğu gözlemlenmiştir. Klinikte, bu özel fizyolojik durumun sayısal olarak anlaşılmasına duyulan ihtiyaçtan yola çıkarak geç gebelik dönemiyle yenidoğan sürecini kapsayan fetal dolaşım ve solunum sisteminin LPM'ini geliştirdik.

Birinci uygulamada, fetal hayattan yenidoğan dolaşımına geçiste, kordon klemplenlenmesinin erken veya geç (sirasiyla, EKK ve GKK) gerçekleştirilmesinin ventriküler ve solunuma dair performans kriterleri üstündeki etkilerinin karşılaştırılmalı olarak inceledik. Oluşturduğumuz modelin gerçeğe uygunluğunu klinik data kullanarak onayladık ve kordon klempleme prosedürlerinin kan akış dinamikleri ve solunum gazları üstündeki etkilerini tahmin etmede kullandık. Klinik verilere dayanarak modellenen zamana bağlı değişen direnç fonksiyonları geçişsel dönemdeki damarsal donüşümleri simule etmek icin kullanıldı. GKK sonucunda gerçekleşen plasental transfüzyon (53 ml) neonatal kan hacmini 19.3% artırdığı gözlemlendi. Artan kan hacminin, EKK'yle karşılaştırıldığında, sol ve sağ preload (kulakçık) basınçlarında % 32 ve % 73 lik bir artış sağladı gözlemlendi , böylece kalp debisinde (KD) % 20'lik bir artış sağlandı (KD_{EKK}=1148 ml/dk: KD_{GKK})=1379 ml/dk). Geliştirdiğimiz model *in vivo* dinamik kan akış paternlerini gerçeğe uygun olarak tahmin etmekte başarılı oldu. Akciğer solunumunun sorunlu başlaması veya solunum başlangıcının gecikmesi durumunda, GKK sayesinde plasental oksijenasyonun sürdürülebildiği gösterildi. Aynı koşullar altında, EKK sırasında oksijen satürasyonlarında %20 -%25'lik ciddi bir düşüş gözlemlendi. Sonuç olarak, kan hacmini artırması ve plasental solunumu sürdürmesi sayesinde, GKK'nin fetalden yenidoğan dolaşımına geçiş sırasında kan akış dinamikleri üzerinde ciddi derecede destekleyici etkisi gösterilmiştir.

İkinci uygulama, maternal hiperoksijenasyon tedavisinde, artan kan oksijen satürasyonuna bağlı olarak gelişen pulmoner ve ductus arteriosus (DA) vazoaktivitenin HSKS'da aortik akış dinamikleri üstündeki etkisinin parametrik incelemesine adanmıştır. Fetal HSKS (taban model), az gelişmiş sol kalp ve aortayi yansıtacak şekilde modellendi. DA'daki vazokonstriksiyon DA'nın akış direncini artırarak (maksimum taban modelin % 1600'ne çıkarılmıştır→ capta yarılanma); pulmoner vazodilatasyon pulmoner vasküler direnci (PVR) azaltarak (maksimum taban modelin % 25'ine düşürülmüştür) modellendi. DA'daki vazokonstriksiyon ve pulmoner vazodilatasyonun sol ventriküler debiyi önemli derecede artırdığı gözlemlendi. Modeldeki maksimal hiperoksijenasyon şartları altında (DA direnç 1600%, PVR %25), asendan aorta ve transvers aortik kaviste pulsatil ve ortalama akış debileri iki kat arttı. Asendan aortada hesaplanan Pulsatil index (PI) bütün simülasyon koşullarda yaklaşık olarak sabit kaldığı gözlendi (bu gözlem Pulsatil akışın ortalama akışla eşit derecede etkilendiğini gösterir). DA'deki PI'n artan DA direnci ve azalan PVR'la azaldığı gözlemlendi.

Bölüm 1'de LPM'e Giriş sunulmuştur. Bölüm 2, Bölüm 3 ve Bölüm 4'te LPM'de kullanılan kan akış ve solunum denklemlerinin teorik ve nümerik incelemesi verilmiştir. Bölüm 5'te fetal dolaşım sisteminin LPM'i oluşturulmuş ve klinik verilerle gerçekliği gösterilmiştir. Bölüm 6 ve Bölüm 7'de sırasıyla göbek kordon klempleme zamanına bağlı yenidoğan akış dinamikleri incelemesi ve maternal hiperoksijenasyon tedavisinin uygulamaları sunulmuştur.

ACKNOWLEDGEMENTS

Foremost, I would like to express my sincere gratitude to my advisor Prof. Kerem Pekkan for the continuous support of my M.Sc. study and research, for his patience, motivation, enthusiasm, and immense knowledge. His guidance helped me in all the time of research and writing of this thesis. I could not have imagined having a better advisor and mentor for my M.Sc. study.

Besides my advisor, I would like to thank the rest of my thesis committee: Prof. Metin Muradoğlu, and Dr. Ahmet Şaşmazel, for their encouragement, and insightful comments.

My sincere thanks goes to Dr. David J.R. Hutchon and Dr. Ahmet Şaşmazel for stimulating the clinical questions that are covered in this thesis, and for their endless support, knowledge, and motivation. I would also like to thank Dr. William J. Kowalski for helping me immensely in the realization of this thesis: the numerical model in this study is based on his Ph. D. research. My sincere thanks also goes to Dr. Bradley B. Keller, and Dr. Ali Rıza Karacı for the inspiring discussions and sharing their expertise in the field during our meetings.

I thank my fellow labmates in Pekkan Cardiovascular Biofluids Group: Şenol Pişkin, Selda Göktaş, Samir Donmazov, Sezin Nargül, and Fazıl Emre Uslusoy for being my brothers(sisters)-in-arms, and for all the fun we have had in the last two years.

I would like to thank The Scientific and Technological Research Council of Turkey (TÜBİTAK-2210) for supporting me financially during the course of my M.Sc. study.

Last but not the least, I would like to thank my family: my parents Selahattin and Lütfiye Yiğit, my brother Batu, and my lovely fiancée Deniz for her patience, her care and her love.

TABLE OF CONTENTS

List of Tables

List of Figures

Chapter 1

Introduction

1.1 Anatomy of the adult and fetal circulation in human:

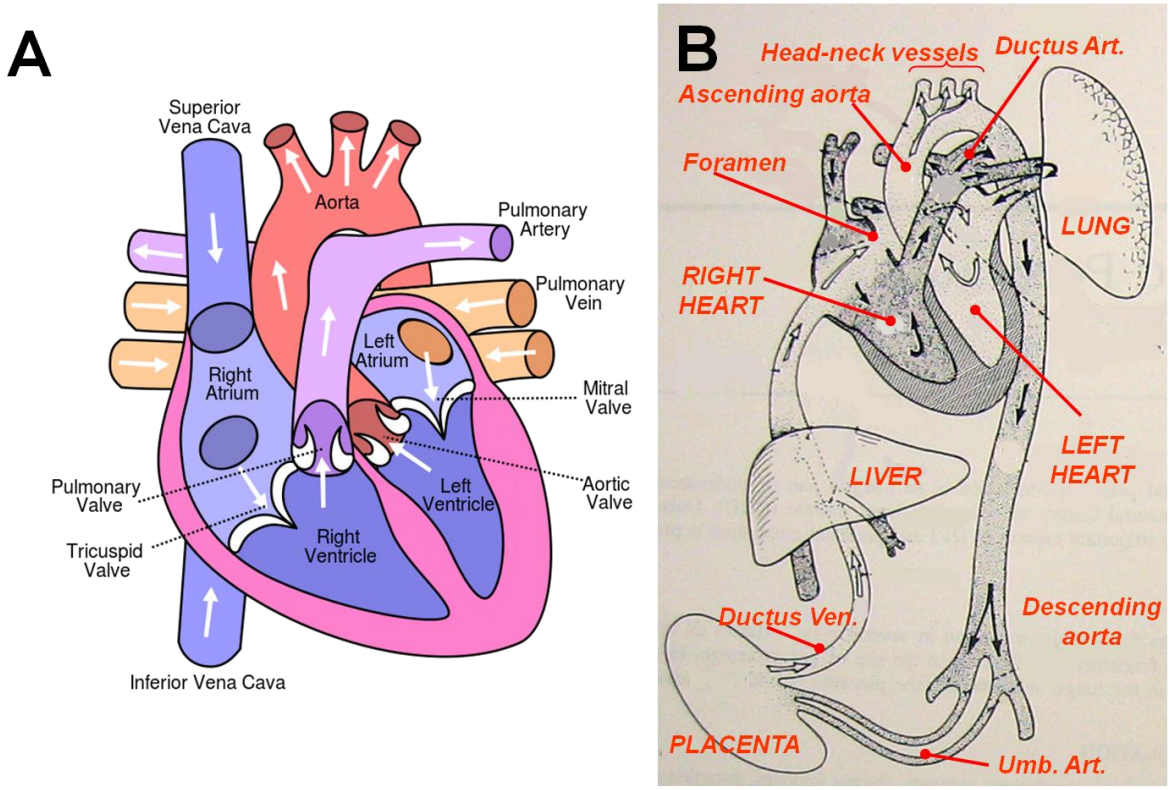

Figure 1.1 Anatomy of the adult heart (A) and the fetal circulation (B)

Adult mammalian heart has four distinct chambers: two atria (left and right) and two ventricles (left and right) that are completely separated from each other by ventricular walls (septum) (Figure 1.1A). Atria and ventricles are muscular structures that can generate pressure and flow in order to pump the blood through the capillary beds of organs and muscles. Ventricles are the main pumps of the heart, meanwhile atrial pumping helps filling the ventricles. Cardiac valves enable the heart to pump the flow in a single direction. Left atrium receives the

oxygenated blood from the pulmonary veins. Left atrium is connected to the left ventricle left ventricle via the mitral valve that allows the passage of flow from the left atrium to the left ventricle. Left ventricle pumps the blood to the ascending aorta through the aortic valve. After traveling the systemic circulation deoxygenated blood arrives at the right atrium through the superior and inferior vena cava. Right atrium is connected to the right ventricle via the tricuspid valve. In turn, right ventricle pumps the deoxygenated blood to the pulmonary circulation through the pulmonary valve.

Arterial vessels emerge from both sides of the heart and branch into smaller arteries that conduct and distribute the blood to the capillary beds that carry nutrients and oxygen to the tissues and organs. Ascending aorta emerges from the left ventricle. The aorta makes a downwards bending arch, hence this section of the aorta is called the aortic arch. Head-neck vessels emerges upwards from the aortic arch that connect to the brachiocephalic arteries. Head neck vessels maintain the blood flow to the head and brain. Descending aorta distributes the blood flow to the lower organs of the body. Some of the important organs are the liver, the intestines, the kidneys, muscles, bones, and skin. Coronary arteries emerge from the aortic root (the base of the aorta very close to aortic leaflets when they are open) and feed the heart. At the pulmonary side, a single main pulmonary artery emerges from the right ventricle, and then it divides into two pulmonary arteries that feed the two lungs.

In fetal circulation (Figure 1.1B), exchange of nutrients, O2, CO2, etc. with the mother takes place at the placenta, which is connected to the systemic circulation of the fetus via umbilical arteries and umbilical vein. Partially oxygenated blood of the fetus flows through the umbilical arteries into the placenta where it is oxygenated. Blood leaves the placenta through the umbilical vein and flows into the hepatic circulation. Ductus venosus is located at the intra-

abdominal side of the umbilical vein and it is connected to the inferior vena cava. Ductus venosus shunts some of the oxygen carrying umbilical vein blood directly to the left atrium in order to increase the oxygen content of the systemic arterial blood. *In utero*, pulmonary circulation is found in a collapsed state. For this reason, blood flow from the right ventricle bypasses the lungs, and it is shunted through the ductus arteriosus into the systemic circulation. Ductus arteriosus connects the pulmonary artery to the proximal descending aorta. Blood flow through the ductus arteriosus is mainly directed to the descending aorta and supplies the lower organs. However, in some cases, some of the ductus arteriosus flow may pass through the aortic isthmus (aortic section found between the head neck vessels and the connection point of ductus arteriosus) and supply the head-neck vessels. Since the left ventricle does not receive the pulmonary venous blood, left ventricular filling is maintained through an opening (foramen) between the right and left atrium, called the Foramen Ovale. Foramen Ovale allows the passage of flow from the right to the left side of the atria, but prevents flow to the other way round.

At birth, pulmonary circulation expands with the first breath and pulmonary blood flow increases rapidly. Since placenta is no longer required, the umbilical cord is either cut immediately or cut after some delay (delayed clamping is advised for at least 30-60 seconds). During the first week following birth, ductus arteriosus and ductus venosus slowly close under the effect of increased oxygen tension in the circulation and with the lack of secretion of vasodilatory prostaglandins. The lack of complete closure of ductus arteriosus is a pathological state and it is called patent ductus arteriosus (PDA). With the gradual closure of ductus arteriosus and with the simultaneous decrease in pulmonary vascular resistance, systemic blood pressure gradually increases and pulmonary blood pressure decreases. With the functional closure of

ductus arteriosus, pulmonary and systemic flow rate (i.e. left and right ventricular output) becomes equal to each other and remains equal unless a systemic-to-pulmonary shunt develops.

Information on the fetal circulation and events related to the transition from fetal to neonatal circulation can be viewed in detailed reviews by Kiserud T. [1], by Rudolph A.M. [2, 3], and by Friedman and Fahey [4].

Aorta branches into smaller arteries, which branch into smaller arterioles. Arterioles then branch into capillaries where nutrient and gas exchange between the blood and the tissues take place. Capillaries are the smallest unit of the vascular structures and capillary beds practically span the whole body volume as a network. Then capillaries merge into venules, those merge into veins that are connected to the atria. Each organ/tissue has very distinct vascular structures specific to that organ or tissue.

Arteries (arterioles) and veins (venules) are characterized by their relatively large diameter and flexible vessel walls. On the other hand, capillaries have diameters about the order of a red blood cell and have rigid walls (inflexible). Due to the high flow resistance of the capillary beds, arterial vessels are subjected to high blood pressures maintained by the heart to push the blood through the capillaries. Thick flexible walls of arteries are mainly consisted of elastin and collagen. Elastin provides resilience to the vessel wall; meanwhile collagen provides stiffness to the vessel wall when vessels distend under high pressures. This prevents the damage from overextension under high blood pressures.

As a fluid system, blood flow in the cardiovascular system obeys the laws of mass conservation, momentum conservation, and energy conservation. Since the vessel walls are elastic, constitutive equations of the vessel walls introduce additional constraints that influence

the blood flow. To approach the cardiovascular system from a mechanistic perspective, we need to understand the relation between forces that exist in the cardiovascular system: Aorta and arteries are flexible and act as a reservoir to buffer the pulsatility of the flow from the heart. Due to the large diameter and the elastic wall of the aorta and arterial vessels, inertial flow and vessel elasticity are dominant over the viscosity of blood. On the other hand, due to their rigid walls and small diameters, flow in the capillaries is predominantly viscous, where elastic and inertial effects are negligible. The physiological task of the venous vessels is to serve as a reservoir into which capillary blood collects before flowing into the heart. To serve effectively as a reservoir, veins have thin and highly flexible walls that can distend easily under small increases in blood pressure. Blood flow is relatively steady in the venous circulation. As a result, inertial effects are small compared to the viscosity of blood flow and the elastic (compliant) characteristic of the venous vessel wall.

1.2 Mathematical modeling of the cardiovascular system: an introduction to Lumped Parameter Models

Lumped parameter models, assume a uniform distribution of pressure, flow, and volume within any compartment (organs, vessels) of the model (thus referred as zero-dimensional), compared to the variation of these parameters in space in higher dimensional models.

Since the discovery of Windkessel effect by Otto Frank in 1899 to explain the decay of arterial pulse pressure [5], zero dimensional models have been an essential tool to study and understand the global dynamics of the cardiovascular system.

Windkessel model was first devised to explain the arterial pressure decay from systole until diastole and the almost steady flow in the capillaries even though the ventricular output is pulsatile. Frank saw the similarity between the “windkessel” used by firefighters and the arterial

system (Figure 1.2). A model incorporating a resistance (*R*, representing the viscous dissipation in the peripheral bed) and a compliance (*C*, representing the elastic distension of the arteries) was able to show both the exponential decay of arterial systolic pressure and the smooth peripheral flow observed during the diastole. Since this model involved two parameters to describe the arterial system, it was called Windkessel-2 or in short WK2. WK2 is perhaps the simplest representation of the arterial system. Windkessel model and its extensions have been extensively studied and reviewed by Westerhof et al. [6] and others. Westerhof *et al.* extended the WK2 to three-elements with the addition of "input impedance" to account for the high frequency characteristics of the proximal aorta, thus called WK3.

A large number of additions and improvements on the classical windkessel such as the incorporation of a venous pressure, ventricular elastance function, and ventricular valves to generate arterial flow [7-9], the inclusion of a fourth inertial element (*L*) (WK4) [10] and the incorporation of a pressure-dependent arterial compliance [11] can be found in the literature for interested readers [6, 12]. Windkessels are important for us in the sense that they provide the basis for more detailed multi compartment LPMs.

In windkessel models, the entire cardiovascular segment under consideration is lumped into a single block, thus distribution of parameters in different segments of the circulation cannot be investigated. In multi-compartment models, vasculature is partitioned into a desired number of components, and each of these components has their own compliance (*C*), resistance (*R*) and inertance (*L*) parameters determined by the local vascular structure and characteristics. For instance, arterial segments can be modeled with a RLC compartment since all effects are dominant in the flow dynamics, capillaries can be modeled with pure resistive elements since elastic and inertial effects are negligible, and veins can be modeled with RC compartments

regarding their blood flow-vessel wall characteristics that were discussed in the first section of this chapter. The partitioned vessel segments (compartments) are connected together to form whole body circulatory networks. A detailed review on one- and zero-dimensional models of the blood flow in the cardiovascular system by Shi *et al.* [12] can be found in the literature for more information.

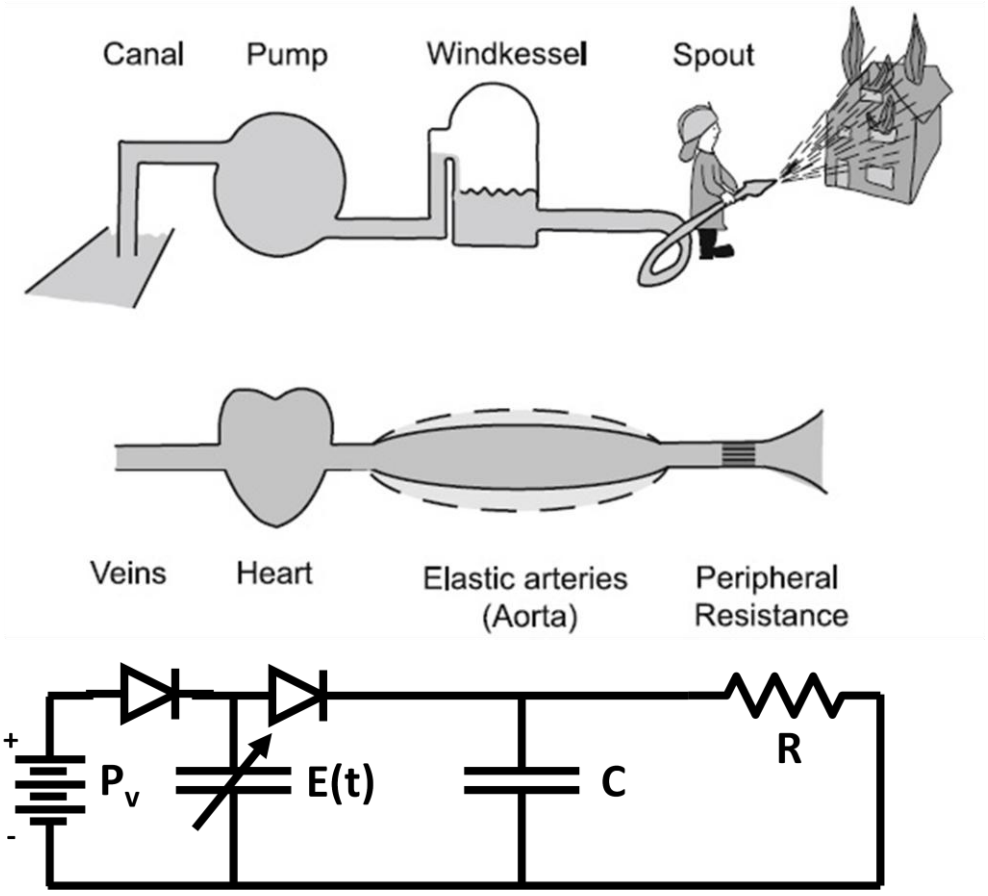

Figure 1.2 "*The concept of Windkessel. The air reservoir is the actual Windkessel, and the large arteries act as the Windkessel. The combination of compliance, together with aortic valves and peripheral resistance, results in a rather peripheral flow.*" (adapted from Westerhof's review paper [6]). Electrical circuit representation of the two-element windkessel extended to include the left ventricle ventricle where P_v is the venous pressure, $E(t)$ is the time-varying elastance function of the left ventricle, C is the compliance of the arterial vessels, and R is the peripheral resistance.

For the interested readers, full models for the systemic arterial network by Noordergraaf *et al.* [13], and Avolio [14] are present in the literature. Tu and Peskin [15] developed a versatile framework for the construction of cardiovascular models with customized network configurations using time-varying ventricular functions, compliance chambers, resistances and valves.

1.3 Lumped parameter models of the fetal circulation

LPMs have been used extensively for the study of fetal circulation and congenital heart defects (CHD) where experimentation *in vivo* is much difficult. Applications of LPMs in the field range from investigation of normal fetal circulation [16, 17], pre-op and post-op investigations of CHDs [15, 18-23]; *in utero* gas exchange [15, 24, 25]; study of fetal shunts [26]; studies of intrauterine growth restricted fetal circulation [27, 28]; transition from fetal to neonatal circulation [29]. Besides pure zero-dimensional models, LPMs are used together with three dimensional simulations to impose realistic boundary conditions [30].

1.4 Objectives: applications of fetal LPM to clinical interventions

In this thesis paper, my objective is to develop a detailed LPM of the fetal circulation incorporating the hemodynamics and respiration, and to apply the developed methodology to the investigation of two clinical interventions:

1) The effect of umbilical cord clamping on the hemodynamics and gas exchange of the transition from fetal to neonatal circulation.
2) The impact of maternal hyperoxygenation therapy on steady and pulsatile flow dynamics in the ascending aorta, aortic isthmus and ductus arteriosus of hypoplastic left heart syndrome fetus.

1.5 Organization of this book:

The present dissertation is organized in two parts that spans seven chapters. The first part is devoted to the lumped parameter models of the fetal circulation. Chapter 1 is Introduction,

Chapters 2 to 4 are devoted to the methodology of LPM, namely, ventricular models, theoretical and numerical framework of hemodynamic and respiration/gas exchange lumped parameter model. In Chapter 5, lumped parameter model of the fetal circulation is presented. In the second part of the thesis, we present two applications of the fetal LPM to the investigation of the clinical pre- and perinatal interventions. Chapter 6 is devoted to the modeling of transition from fetal to neonatal circulation and investigates the effect of immediate and delayed cord clamping on the perinatal hemodynamics and gas exchange. Chapter 7 is devoted to the investigation of the impact of ductus arteriosus resistance and pulmonary vascular changes on the steady and pulsatile flow dynamics at the underdeveloped aorta of fetal HLHS circulation in the context of a pre-surgical improvement therapy. Finally, Conclusion is presented.

Chapter 2

Ventricular models

2.1 Concept of elastance function:

Heart operates in a cycle and, pressure-volume (PV) diagrams are used commonly to study the performance and operating characteristics of ventricles. Figure 2.1A displays a representative example of a PV loop sampled during a single cardiac cycle. As shown in the figure, cardiac cycle is consisted of four distinct phases: the filling phase (diastole) (D-A), the isovolumetric contraction phase (A-B), the ejection phase (systole) (B-C), and the isovolumetric relaxation phase (C-D). This sequence also marks four important time points: initiation of diastole (D), end-diastole (A), initiation of systole (B), and end-systole (C).

Work of Suga and Sagawa [31] and Suga et al. [9] introduced the concept of time-varying elastance ($E(t)$) that represents the time course of ventricular stiffness. This elastance function is derived from the proportionality between intraventricular pressure and volume ($E(t) = \frac{dP}{dV}$). The concept of time-varying elastance function is very useful in the study of ventricular dynamics and in the modeling of ventricular function. This methodology assumes that all isochrones (i.e., curves that connect pressure-volume data occurring at the same time in cardiac cycle) are linear and have a common volume intercept (Figure 2.1B). The peak value of the time-varying elastance approximates the slope of the end-systolic pressure-volume relationship (ESPVR) (the steepest isochrone), which serves as an index for cardiac contractile function. The minimum value of the time-varying elastance approximates the slope of the end-diastolic pressure-volume relationship (the most flat isochrone), which serves an index for cardiac filling function. Most importantly, elastance function is independent of the ventricular pre-load (end-diastolic volume)

and afterload (arterial pressure) under physiological limits, therefore once determined it can be used for a variety of load settings.

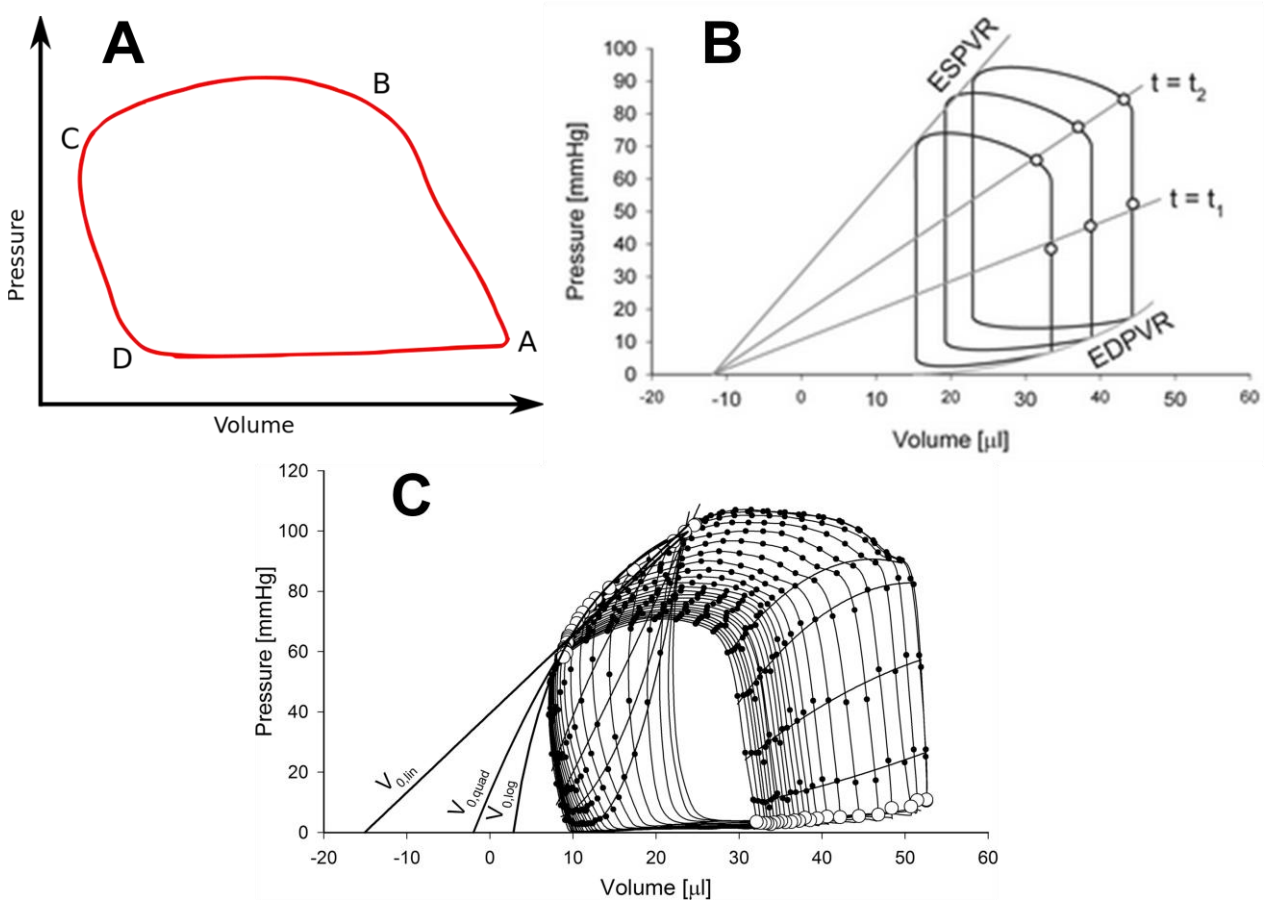

Figure 2.1 Representative example of a pressure-volume (PV) loop of a mouse left ventricle during a single cardiac cycle (A), PV loops under different load states showing the end-systolic and end-diastolic pressure-volume relations (ESPVR and EDPVR, respectively) (B), nonlinear PV isochrones (lines connecting data acquired at the same time instant during each cardiac cycle –black dots- after the onset of systole –white dots) constructed under varying filling pressures. B and C are taken from Claessens *et al.* [32].

Other studies showed that the normalized elastance function is similar across mammalian species [33], and the shape of the normalized elastance function is conserved under different pathological states for humans [34]. Nonlinear approaches to the analysis of PV isochrones are investigated in the literature [32] (Figure 2.1C).

2.2 Review of six isochrone models for the simulation of instantaneous pressure-volume relation of left ventricle [35]:

This section is based on the comparative study of six isochrone models by Lankhaar *et al.* [35]. Isochrone models were fit to time-resolved pressure-volume loop measurements from the left ventricle, and simulations were performed on a three-element Windkessel of the arterial system. Windkessel parameters were fit using measured arterial pressures and stroke volumes. Performance and fitting accuracy of the isochrones models were assessed by the comparison of measured and simulated PV loops with Akaike Information Criterion (AIC) (a score based on accuracy (sum of squared residuals between the measured and simulated PV data) and the number of required parameters for simulation) and the Hamming distance (a measure for geometric shape similarity). The isochrone models under consideration are not strictly derived from the physics and physiology of ventricles, but they represent the time dependent behavior of isochrones through fitting experimental data. These models are: 1) Linear model with fixed volume intercept (LinFix), 2) Linear model with variable (free) volume intercept (LinFree, 3) Langewouters Model (Langew), 4) Sigmoid Model (Sigm), 5) Shroff Model, 6) Burkh Model. Models 2-5 take into account the nonlinearities of PV isochrones with different approaches, while Model 1 (LinFix) is the classical linear model that is described in the previous section. Figure 2.2 shows the isochrones models.

1) *LinFix*: The classical model relates ventricular pressure (*P(t)*) and volume (*V(t)*) according to E2.1, where E(t) is the elastance and V_0 is the fixed volume intercept (volume at zero trans-mural pressure).

$$P(t) = E(t)[V(t) - V_0] \tag{E2.1}$$

2) *LinFree*: This model is similar to the classical model, but the volume intercept is allowed to vary with time E2.2.

$$P(t) = E(t)[V(t) - V_0(t)] \tag{E2.2}$$

3) *Langew*: This model is originally developed to describe PV relation in arteries [36], but translated here for ventricles. The model is given in E2.3, where $P_0(t)$ and $P_1(t)$ are two time-varying parameters, and V_m is a fixed maximum physiological volume, of which the value needs to be estimated by assumption.

$$P(t) = P_0(t) + P_1(t)tan\pi\left(V(t) - \frac{1}{2}V_m\right)/V_m \tag{E2.3}$$

4) *Sigm*: This model is formulated to fit the sigmoid appearance of observed isochrones. Details of model can be viewed at the original publication.

5) *Shrof*: This model incorporates the effect of resistance to flow of the ventricle on the PV relation. An resistive term is added to E2.1 to obtain E2.4 (ρ: resistance proportionality factor, $\dot{V}$: ventricular outflow)**.**

$$P(t) = E(t)[V(t) - V_0]\left(1 - \rho\dot{V}\right) \tag{E2.4}$$

6) *Burkh*: This model assumes a linear ESPVR, an exponential (volume stiffening) EDPVR, and a smooth transition for the isochrones in-between. Details of model can be viewed at the original publication.

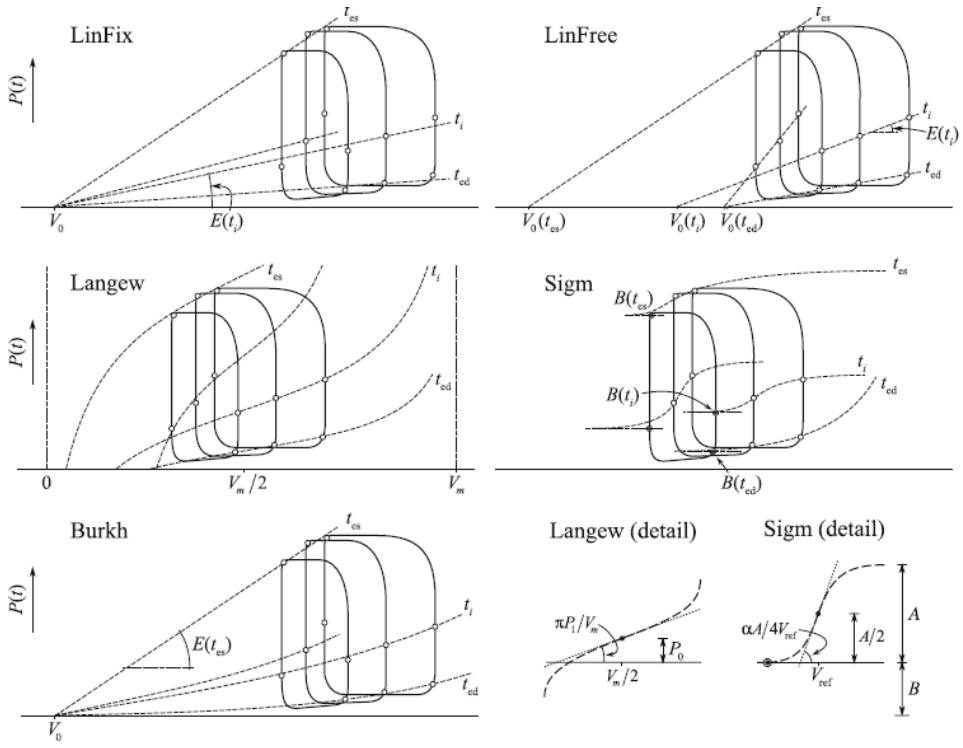

Figure 2.2 Isochrone models. "The isochrone models compared in this study with the meaning of their parameters. PV-loops representing three different preload-conditions are shown. Open circles denote corresponding (isochronal) points in the cardiac cycles. An isochrone (dashed line) is shown for each of the four cardiac phases.". Adapted from [35].

The LinFree model was found to be the best choice for simulating pressure and volume as a function of time. If only the shape of the PV-loops is important, the LinFix and Burkh model are the best options. Authors conclude that, despite the observed nonlinearity in the isochrones linear models suffice for simulations of PV-loops.

An important shortcoming of the LinFree model was its poor performance in simulating the diastolic filling. The model is insufficient because small changes in filling pressure lead to unrealisticly large end-diastolic volume changes due to a very flat EDPVR arising from the constrained fitting process. In LinFix model, the slope of the EDPVR approaches zero, which indicates that small changes in preload pressures would be accompanied by large changes in the end-diastolic volume. This drawback was critical for our simulations since we were simulating

dynamic changes in the circulation where large changes in the preload pressures take place. According to the study, the LinFree model does not show this unrealistic diastolic behavior, and is advantageous for it has a limited number of parameters.

2.3 Heart model of the fetal LPM:

A time-varying elastance model with variable volume intercept was developed for the ventricular chambers, providing an improved representation of the end-diastolic pressure volume relationship [35]. A classical time-varying elastance model (LinFree) [9] was used for the atria. In both models, activation functions govern the systolic and diastolic contraction properties of the myocardial muscle. For the left ventricle (LV) and the right ventricle (RV), activation functions for the time varying elastance ($E(t)$) and volume intercept ($V_0(t)$) are adopted from the LV PV isochrones of sheep [35] and scaled for the human fetus. The four heart valves and foramen ovale are modeled as unidirectional resistance. We made sure that small amounts of regurgitative flow A sensitivity analysis yield that small regurgitation flow has a negligible effect. Maximum percent change in combined cardiac output (CCO) was 2% when the combined regurgitation was 33%).

2.4 Theoretical and numerical framework of elastance models employed in the LPM:

Ventricular and atrial function are assumed to be periodic: $f(t) = f(t + T)$. Period T is fixed and equal to the duration of a cardiac cycle.

Ventricular function is governed by the time varying elastance function with a variable volume intercept E2.5 [35]. Compliance is the inverse of elastance, therefore E2.5 can be written as E2.6.

$$P(t) = E(t)[V(t) - V_0(t)] \quad \text{(E2.5)}$$

$$V(t) = C(t)P(t) + V_0(t) \quad \text{(E2.6)}$$

Time dependent linear elastance $E(t)$ and volume intercept $V_0(t)$ curves are obtained by digitizing previously reported $E(t)$ and $V_0(t)$ curves for the LV function of adult sheep (approximate weight 35 kg) [35]. Curves are normalized with an approach described in previous studies [8, 34] to obtain $C^*(t), {V_0}^*(t)$. Normalized ventricular function is then scaled for the human fetus (3.5kg) by multiplying with desired peak values (ΔC: determinant of end-diastolic filling, ΔV_0) and adding the offset (C_{offset}: measure of contractility, $V_{0,offset}$) to match proper stroke volumes, ejection fractions [37], systolic and diastolic pressures [38], and PV loop shapes [35] (comparison of PV loop shape was done for LV only) (E2.7 and E2.8). E2.9 describes the construction of the $C(t)$ and $V_0(t)$ using the n-th coefficients a_n and b_n of Fourier interpolation. Same normalized $C^*(t), {V_0}^*(t)$ functions were used for the LV and RV.

$$C(t) = \Delta C.\, C^*(t) + C_{offset} \quad \text{(E2.7)}$$

$$V_0(t) = \Delta V_0.\, V_0^*(t) + V_{0\,offset} \quad \text{(E2.8)}$$

$$C^*(t), V_0^*(t) = \sum_{n=0}^{15} \left[a_n \cos\left(2\pi n \frac{t}{T}\right) + b_n \sin\left(2\pi n \frac{t}{T}\right) \right] \quad \text{(E2.9)}$$

Atrial function is governed by the classical elastance model [9]. The value of atrial compliance transitions between a maximum at the end of diastole (diastole is denoted by the subscript *D*, t=T) and a minimum at the end of systole (systole is denoted by subscript *S*, t=T_S) according to a generalized transition function given by E2.10 that represents the form of the experimentally visualized elastance transition [23]. The behavior of the transition is controlled by the time constants τ_S and τ_D. Time interval (in minutes) between the ventricular and atrial contractions is denoted as φ.

$$C(t)=\begin{cases} C_D\left(\dfrac{C_S}{C_D}\right)^{\frac{1-\exp(-t/\tau_S)}{1-\exp(-T_S/\tau_S)}}, & 0\le t\le T_S \\ C_S\left(\dfrac{C_D}{C_S}\right)^{\frac{1-\exp(-(t-T_S)/\tau_D)}{1-\exp(-(T-T_S)/\tau_D)}}, & T_S\le t\le T \end{cases} \qquad \text{(E2.10)}$$

Chapter 3

Theoretical and Numerical Framework of the Lumped Parameter Model

3.1 Mathematical framework of flow and vessel dynamics

Mathematical framework for the LPM is adapted from Peskin *et al.*'s study [22, 23]. This versatile framework allows the construction of arbitrary lumped parameter circulation networks using resistive and compliance elements. An LPM is created by first defining a number of compartments (nodes) **N**, each compartment has an assigned index i ($i \in \{1, \dots, N\}$). These compartments represent specific cardiovascular segments where the volume (V_i) and pressure (P_i) information are stored (e.g. systemic pulmonary arteries, or veins, ventricles, atria, etc.). Compliance (C_i) is the ratio of the change in volume to the change in pressure E3.1 and it represents the elastic properties of a cardiovascular structure.

$$C_i = \frac{dV_i}{dP_i} \tag{E3.1}$$

If the compliance of a vessel can be assumed constant then the blood volume contained at the compartment i (V_i) minus the vessel volume at zero transmural pressure (unstressed blood volume [1]) ($V_{0,i}$) and P_i are linearly related through C_i as in E3.2. This linear pressure-volume

[1] Stressed blood volume (SBV) is a fraction of the total blood volume, which contributes to the generation of a baseline pressure by pressurizing and distending the vessels. The remaining fraction is called unstressed blood volume (UBV), and it only fills the empty space of vessels and does not contribute to the mean circulatory filling pressure (MCFP). MCFP is the pressure that would be observed in the circulation if the heart was stopped and all pressures reached equilibrium instantaneously. It is an indicator and approximator of the mean ventricular filling pressure; therefore it is important in cardiovascular performance. For more information on the concept of MCFP, reference [83] would be useful. UBV remains as a reserve and can be actively converted to SBV by vasoconstriction of the venules. The reverse also happens by vasodilatation. It should be noted that in our model we did not include the control of reserve blood. Therefore placental volume shift contributes directly to the SBV, thus to the MCFP. MCFP is the initial condition of pressure in our LPM and it is specified as 12 mmHg.

assumption is valid for venous vessels with transmural pressure above ~5mmHg and for arterial vessels in general.

$$V_i = C_i P_i + V_{0,i} \quad \text{(E3.2)}$$

In reality, aorta and systemic arteries (e.g. cerebral arteries, hepatic arteries) are characterized by non-linear elasticity: they got stiffer with increased circumferential strain to prevent instabilities and to protect the vessel against over-distension and rupture under increased transmural pressures [39]. Non-linear pressure-volume relationship of the arterial windkessel is formulated as in E3.3 [6, 11]. Pressure-dependent compliance (*C(P)*) is obtained by taking the derivative of *V(P)* with respect to *P* (E3.4).

$$V_i(P_i) = a_i * (e^{b_i P_i} - 1) + V_{0,i} \quad \text{(E3.3)}$$

$$C_i(P_i) = a_i * b_i * e^{-b_i P_i} \quad \text{(E3.4)}$$

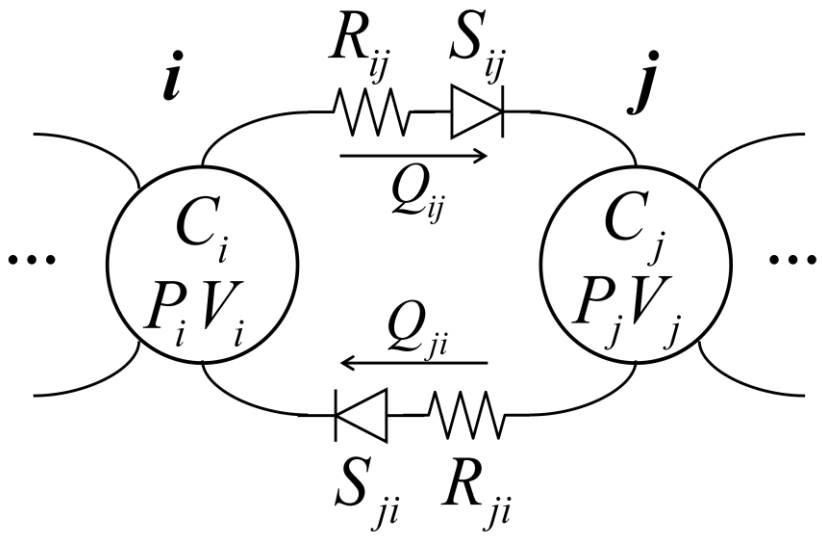

Figure 3.1 Connections between a pair of compliance chambers in the lumped parameter network

Figure 3.1 shows the relation between an arbitrary pair of compliance chambers labeled by their pressures (P_i and P_j). Every such pair in the model is connected by a pair of resistance vessels (R_{ij} and R_{ji}) equipped with valves in series, the two valves of the pair pointing in opposite directions. S_{ij} (having a value of 0 or 1) denotes the state of the valve that allows flow from

compliance chamber *i* into compliance chamber *j*. The instantaneous flow rate from the chamber *i* to chamber *j* (Q_{ij}) is calculated by E3.5. Valve states are modeled as ideal diodes E3.6.

$$Q_{ij} = S_{ij}\frac{P_i - P_j}{R_{ij}} \tag{E3.5}$$

$$S_{ij} = \begin{Bmatrix} 1 & ,P_i > P_j \\ 0 & ,P_i < P_j \end{Bmatrix} \tag{E3.6}$$

Volume conservation of blood at a single node written in E3.7 requires the instantenous volume stored in the compliance chamber to be equal to the difference between the sum of inflow and the sum of outflow.

$$\frac{d(V_i)}{dt} = \sum_{j=1}^{N}\left[Q_{ji} - Q_{ij}\right] \tag{E3.7}$$

Combining E3.7 and E3.5, we obtain the general form of the governing mass conservation equation (E3.8).

$$\frac{d(V_i)}{dt} = \sum_{j=1}^{N}\left[\left(\frac{S_{ij}}{R_{ij}} + \frac{S_{ji}}{R_{ji}}\right)(P_j - P_i)\right] \tag{E3.8}$$

We obtain the governing equation E3.9 for chambers with linear pressure-volume relationship combining E3.8 with E3.2 and E3.7, and E3.10 for chambers with pressure-dependent compliances combining E3.8 with E3.3 and E3.7.

$$\frac{d(C_iP_i + V_{0,i})}{dt} = \sum_{j=1}^{N}\left[\left(\frac{S_{ij}}{R_{ij}} + \frac{S_{ji}}{R_{ji}}\right)(P_j - P_i)\right] \tag{E3.9}$$

$$\frac{d(a_ie^{b_iP_i} + V_{0,i})}{dt} = \sum_{j=1}^{N}\left[\left(\frac{S_{ij}}{R_{ij}} + \frac{S_{ji}}{R_{ji}}\right)(P_j - P_i)\right] \tag{E3.10}$$

3.2 Numerical treatment of the LPM equations

Governing equation E3.8 is discretized with Backwards Euler Scheme giving us E3.11.

$$\frac{V_i^{n+1}-V_i^n}{\Delta t}+O(\Delta t)=\sum_{j=1}^{N}\left(S_{ij}R_{ij}^{-1}+S_{ji}R_{ji}^{-1}\right).\left(P_j^{n+1}-P_i^{n+1}\right) \quad \text{(E3.11)}$$

Backwards scheme is preferred over a Forwards scheme, because in Forward schemes the smallest resistance value in the LPM determines how small the time step size (Δt) is required to be in order to prevent numerical instabilities. In the LPM, valves have resistances that are 1/1000 of the peripheral resistance. Using Backwards scheme prevents this issue without requiring the time step to get smaller when particular resistances are small [23].

E3.9 and E3.10 are discretized to obtain E3.12 and E3.13.

$$\frac{C_i^{n+1}P_i^{n+1}+V_{0,i}^{n+1}-C_i^nP_i^n-V_{0,i}^n}{\Delta t}+O(\Delta t)=\sum_{j=1}^{N}\left(S_{ij}R_{ij}^{-1}+S_{ji}R_{ji}^{-1}\right).\left(P_j^{n+1}-P_i^{n+1}\right) \quad \text{(E3.12)}$$

$$\frac{a_ie^{bP_i^{n+1}}+V_{0,i}^{n+1}-a_ie^{bP_i^n}-V_{0,i}^n}{\Delta t}+O(\Delta t)=\sum_{j=1}^{N}\left(S_{ij}R_{ij}^{-1}+S_{ji}R_{ji}^{-1}\right).\left(P_j^{n+1}-P_i^{n+1}\right) \quad \text{(E3.13)}$$

Due to E3.13, resulting system of equations is non-linear and we cannot use linear solvers. E3.11 is rearranged to obtain the residual (Res) function that is given in E3.14.

$$Res_i^{n+1}=-\left(V_i^{n+1}-V_i^n\right)+\Delta t.\sum_{j=1}^{N}\left(S_{ij}R_{ij}^{-1}+S_{ji}R_{ji}^{-1}\right).\left(P_j^{n+1}-P_i^{n+1}\right) \quad \text{(E3.14)}$$

This *Residual* is a volume error in the numerical solution that should be approximately zero at each time step. Further, we need to control the accumulation of volume error during the course of simulation. The sum of residuals until the time step *n* is added to both sides of E3.14 that gives E3.15. Solving for the roots of E3.15 prevents the accumulation of residuals in a net positive or negative direction.

$$\sum_{t=0}^{n+1} Res_i^t = \sum_{t=0}^{n} Res_i^t - \left(V_i^{n+1} - V_i^n\right) + \Delta t.\sum_{j=1}^{N}\left(S_{ij}R_{ij}^{-1} + S_{ji}R_{ji}^{-1}\right).\left(P_j^{n+1} - P_i^{n+1}\right) \qquad \text{(E3.15)}$$

We used MATLAB's optimization toolbox function "`fsolve`", which uses trust-region dogleg algorithm, to search the roots of the nonlinear system of equations governed by discretized residual function E3.15. At each time step *n*, E3.15 is updated with parameter values that are known (prescribed activation functions) for *n+1*, and the solution at time step *n* is specified as the initial condition for the solution of the system at time step *n+1* through the `fsolve` algorithm.

Chapter 4

Respiratory / Gas Exchange Model

The circulatory and respiratory systems work in unison to deliver oxygen to the systemic tissues. As blood flows through the pulmonary capillary networks, oxygen molecules diffuse from alveoli to the blood stream across the thin alveolar-capillary membranes, increasing the oxygen content of the blood. The diffusion of O_2 is a result of the pressure gradient of O_2 between the O_2 rich alveoli and O_2 deficient capillary blood. O_2 from the alveolar air moves down into the blood, where it binds to hemoglobin (Hb) molecules in red blood cells. Movement of O_2 continues until the partial pressure of O_2 in the air equals the partial pressure of O_2 in the blood, or until the blood has completely passed through the pulmonary capillary. This process is achieved *in utero* through diffusion of oxygen between the fetal and maternal bloods that takes place in the placenta. As blood flows through the systemic circulation, oxygen is consumed through tissue metabolism, lowering the oxygen content of blood. Both blood flow and ventilation must be matched in order to maintain the metabolic demands of the tissue.

4.1 Oxygen-hemoglobin dissociation curve

O_2 carrying capacity of blood is determined by the concentration of hemoglobin in blood (hematocrit, *[Hb]*) and the affinity of hemoglobin to bind O_2. The affinity of hemoglobin to bind O_2 molecules can be measured by the partial pressure of O_2 required to achieve 50% saturation ($P_{50,O2}$). Saturation is calculated by dividing the current [O_2] to the maximum [O_2] ($[O_2]_{max}$) that blood can achieve, when all hemoglobins are bound with 4 O_2 molecules. One gram of hemoglobin can at most carry 1.34 ml O_2 when all 4 O_2 binding sites are occupied.

Oxygen-hemoglobin dissociation curve relates the oxygen saturation (SO_2) to oxygen tension (partial pressure of O_2 in blood: P_{O_2}) and it has a sigmoid shape in which oxygen tension increases faster with small increments in saturation SO_2 when high SO_2 levels are reached. Hill's equation is used to represent the oxygen-hemoglobin curve E4.1. Hill's equation does not have a physical meaning and only represents the shape of the observed dissociation curve.

$$P_{O_2} = H\left(\left[O_2\right]\right) = P_{50}\left(\frac{\left[O_2\right]}{[Hb]\times 1.34 - \left[O_2\right]}\right)^{1/2.7} \tag{E4.1}$$

Fetal circulation has certain adaptations to increase the oxygen intake and carrying capacity such as an increased *[Hb]* (fetal *[Hb]=17.5g/dl*) and a lower P_{50} due to a special fetal hemoglobin (fetal P_{50}*=20mmHg*) compared to adult circulation (adopted values for maternal adult *[Hb]=12g/dl*, P_{50}*=26.6mmHg*) [3, 40]. Therefore we use H_F and H_M to indicate fetal and maternal Hill equation.

In the following paragraphs, we will use pulmonary respiration terminology for ease; placental gas exchange will be expanded over the pulmonary gas exchange material.

4.2 Gas Transport Equations

Oxygen is transferred between circulatory compartments due to convection by the flow of blood. Therefore, gas transport equations are coupled to the solution of the hemodynamic model.

$$\frac{d(V_i\left[O_2\right]_i)}{dt} = \sum_{\substack{j=1 \\ Q_{ji}>0}}^{N}\left[Q_{ji}[O_2]_{ji}\right] + \sum_{\substack{j=1 \\ Q_{ij}>0}}^{N}\left[-Q_{ij}[O_2]_i\right] - \dot{M}_i \tag{E4.2}$$

$$[O_2]_{ji} = [O_2]_j + \frac{\dot{O}_{2,in}}{Q_{ji}} \quad \text{(E4.3)}$$

The mass balance of oxygen in a given compliance chamber can be described by E4.2 (Figure 4.1) [15], where V_i is the volume of blood in chamber i, $[O_2]_i$ is the O_2 concentration of blood in chamber i, $[O_2]_{ji}$ is the O_2 concentration of the blood inflowing to chamber i from chamber j, $Q_{ji} > 0$ denotes flow into chamber i that originates from chamber j, while $Q_{ij} > 0$ denotes blood flow out of chamber i. $[O_2]_{ji}$ is determined by E4.3 where parameters are Q_{ji}, the O_2 concentration of the blood in chamber j ($[O_2]_j$), and the minute O_2 volume intake ($\dot{O}_{2,in}$) through respiration in the lungs or the placenta. The tissue metabolic oxygen consumption in the compliance chamber i (M_i) is extracted from the system. M_i is assumed to be independent of capillary PO_2.

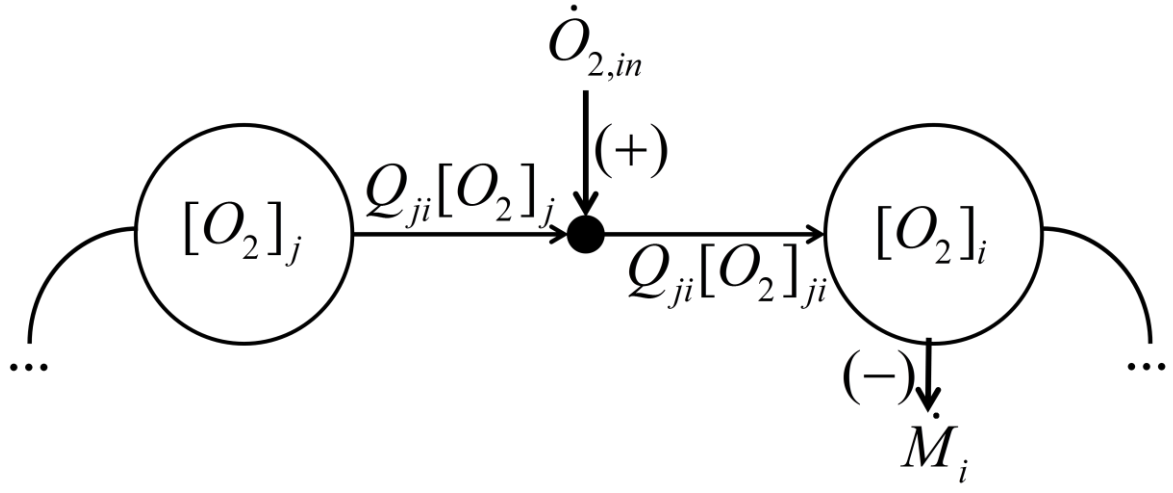

Figure 4.1. O_2 transport between two compliance chambers from chamber labeled j to chamber labeled i. O_2 is carried by blood flow from chamber j to chamber i (Q_{ji}). O_2 intake ($\dot{O}_{2,in}$) takes place during the convection of O2 from chamber j to chamber i and determines O_2 concentration of the flow into chamber i ($[O_2]_{ji}$). Tissue metabolic consumption ($\dot{M}_i$) is extracted from the chamber.

For numerical analysis, E4.2 can be discretized and rearranged to solve for $[O_2]_i$ directly (covered in Section 4.4). An important step in the evaluation of the discretized form of $[O_2]_i$ is the calculation of $[O_2]_{ji}$. For chambers other than the pulmonary veins/umbilical vein, the value of $[O_2]_{ji}$ is equal to $[O_2]_j$. Before blood enters the pulmonary veins, however, it must pass through the lung, where oxygen is added. $\dot{O}_{2,in}$ is determined by gas exchange in the lungs and the placenta.

4.3 Gas Exchange in the Lungs

Arterio-venous O_2 uptake is determined by flow rate and partial pressure of oxygen (PO_2) in the arteries of the respiratory organ, hematocrit, oxygen-hemoglobin dissociation curve, ventilation/perfusion ratio (V/Q), and the diffusion efficiency (γ) of the gas exchange unit.

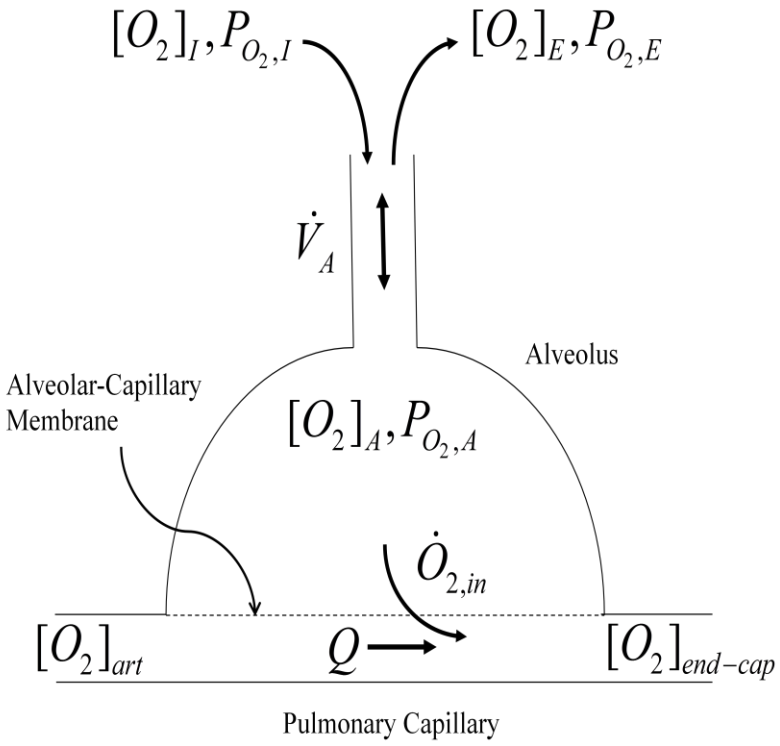

Figure 4.2 Representative diagram of gas exchange in the alveolus-capillary unit.

Figure 4.2 depicts the oxygen gas exchange in one alveolar-capillary unit, where V_A is alveolar volume, $\dot{V}_A$ is the volume flow rate into/out of the alveolus, Q is capillary flow rate, and subscripts *art*, *end-cap*, *A*, *I*, *E* denote belongingness of $[O_2]$ and P_{O_2} parameters to arterial (entrance) and exit (end) sides of the capillary, and alveolar, inspired, expired air volumes, respectively. Mass balance of oxygen in a single alveolar-capillary unit can be described by E4.4. In the case of pulmonary circulation, subscript *j* and *ji* in E4.4 corresponds to the pulmonary artery, and to the flow at the exit of pulmonary capillaries after oxygenation takes place. + and – signs over the $\dot{V}_A$ term indicates that if the sign is + that term can only take positive values or it is equal to zero, and if the sign is - that term can only take negative values or it is equal to zero .

$$\frac{d(\mathrm{V}_A[O_2]_A)}{dt} = \dot{V}_A^+[O_2]_I + \dot{V}_A^-[O_2]_E - Q\left([O_2]_{ji} - [O_2]_j\right) \tag{E4.4}$$

Here, we introduce a number of assumptions to derive the gas exchange equations in the LPM: 1) *steady state*: left hand side of E4.4 is ignored, also inhalation and exhalation of air takes place simultaneously and their magnitudes are equal to each other ($V_A^+ = |\dot{V}_A|$ and $V_A^- = -|\dot{V}_A|$, or we will refer to the ventilation simply $\dot{V}_A$); 2) Alveolar ventilation/ perfusion ratio ($\dot{V}_A/Q$) is a constant *r*; 3) expired air is a sample of alveolar air ($[O_2]_E = [O_2]_A$) and do not mix with inspired air. Further, we introduce the assumption that $\dot{V}_A/Q$ is constant throughout the lungs (which is also the condition for optimal gas transport [23]) so that we can lump the respiratory function into a single pulmonary compartment, thus lumped ventilation-perfusion ratio is $\frac{\dot{V}}{Q} = r$. These assumptions reduce E4.4 to E4.5.

$$r\left([O_2]_I - [O_2]_E\right) = [O_2]_{ji} - [O_2]_j \tag{E4.5}$$

Two additional assumptions are required for our model: 4) alveolar oxygen behaves like an ideal gas (E4.6) where R is the ideal gas constant and T is the absolute temperature;

$$P_{O_2,A} = [O_2]_A RT \tag{E4.6}$$

5) oxygen-hemoglobin dissociation curve is governed by Hill's equation (E4.1), which is described in the first section of this chapter; 6) equilibrium of alveolar air and capillary blood is determined by a membrane diffusion efficiency parameter (γ), which will be discussed in the following paragraph.

Alveolar/capillary diffusion efficiency for oxygen is specified by the constant γ. E4.7 states that the ratio between the gain (difference) of PO_2 across the inlet ($P_{O_2,j}$) and outlet ($P_{O_2,ji}$) of the pulmonary capillaries to the maximum possible gain of PO_2 (if the capillary and alveolar air were to come to an equilibrium before the blood exits the capillary, $P_{O_2,E} = P_{O_2,ji}$) is a constant γ.

$$\gamma = \frac{P_{O_2,ij} - P_{O_2,j}}{P_{O_2,E} - P_{O_2,j}} \tag{E4.7}$$

The diffusion efficiency for oxygen across the alveolar-capillary membranes is specified by γ_{pul}, which is also the overall diffusion efficiency of the lung. If $\gamma_{pul} = 1$, then PO_2 of capillary blood and PO_2 of alveolar air always equilibrate when the blood exits the pulmonary capillary. If $\gamma_{pul} < 1$, the capillary blood may not equilibrate with the alveolar air resulting in a lower oxygen concentration in the pulmonary veins.

Incorporating E4.5 with E4.1, E4.6 and E4.7, the gas exchange in the lungs can be expressed with E4.8.

$$0 = [O_2]_j - [O_2]_{ji} + r[O_2]_I - r\frac{H_F\left([O_2]_j\right)}{\gamma_{pul}RT} + r\frac{(1-\gamma)H_F\left([O_2]_{ji}\right)}{\gamma_{pul}RT} \tag{E4.8}$$

4.4 Numerical treatment

E4.2 is discretized with Backwards Euler Scheme giving the discretized governing equation E4.9.

$$\frac{V_i^{n+1}[O_2]_i^{n+1} - V_i^n[O_2]_i^n}{\Delta t} = \sum_{\substack{j=1 \\ Q_{ji}^{n+1}>0}}^{N}\left[Q_{ji}^{n+1}[O_2]_{ji}^{n+1}\right] + \sum_{\substack{j=1 \\ Q_{ij}^{n+1}>0}}^{N}\left[-Q_{ij}^{n+1}[O_2]_i^{n+1}\right] - \dot{M}_i \tag{E4.9}$$

Values of V_i, Q_{ji} and Q_{ij} at time steps *n* and *n+1* are known from the hemodynamic LPM. E4.9 is rearranged to calculate $[O_2]_i^{n+1}$explicitly (E4.10).

$$[O_2]_i^{n+1} = \frac{\Delta t \sum_{\substack{j=1 \\ Q_{ji}^{n+1}>0}}^{N}\left[Q_{ji}^{n+1}[O_2]_{ji}^{n+1}\right] - \dot{M}_i + V_i^n[O_2]_i^n}{V_i^{n+1} + \Delta t \sum_{\substack{j=1 \\ Q_{ij}^{n+1}>0}}^{N}\left[Q_{ij}^{n+1}\right]} \tag{E4.10}$$

Since the $[O_2]_{ji}^{n+1}$ term on the right hand side is unknown initially, we guess its value by solving E4.8 with the parameters of known values of time step *n*. Then we calculate the value of $[O_2]_i$ for each chamber using E4.10. E4.8 can be solved for $[O_2]_{ji}$ with the application of the method of bisection [23]. When set to zero, E4.8 forms a continuously increasing function on the interval $[O_2] \in [0, [O_2]_{max}]$, where $[O_2]_{max}$ is the maximal oxygen concentration, i.e. each hemoglobin has 4 oxygen molecules bound. The normal value for $[O_2]_{max}$ is $17.5\frac{gHb}{dl} * 1.34\frac{mlO_2}{dl}$, which was used in this model [41]. Similarly, oxygen saturation is calculated by dividing computed $[O_2]_i$ by $[O_2]_{max}$. After this first iteration, same procedure is repeated until the difference between two consecutive iterations is under a certain tolerance.

4.5 Placental Gas Exchange

Compared to pulmonary respiration, O_2 transfer in the placenta occurs between the maternal uterine and fetal placental capillaries, thus the inverse Hill function of maternal circulation ($H_M([O_{2,\ uterine}])$) governs the relation between the uterine PO_2 and the uterine $[O_2]$. Also, the pulmonary diffusion efficiency (γ_{pul}) is replaced with the placental diffusion efficiency which is denoted as γ_{plac}, resulting in E4.11.

$$0 = [O_2]_j - [O_2]_{ji} + r[O_2]_I - rH_M^{-1}\left(\frac{H_F\left([O_2]_j\right)}{\gamma_{plac}} + \frac{\left(1-\gamma_{plac}\right)H_F\left([O_2]_{ji}\right)}{\gamma_{plac}}\right) \quad \text{(E4.11)}$$

In the case of placental circulation, the value of r in E4.11 is calculated by dividing the uterine blood flow rate at the maternal side, which has a preset value of 600 ml/min [42], with the placental blood flow rate computed by the LPM. Assumptions regarding membrane diffusion efficiency is similar to the pulmonary gas exchange model. Since the resistance to diffusion of the blood-blood barrier is higher than alveolar-capillary membrane, and because of the high metabolic consumption of placenta (60% of the total feto-placental consumption [43]), PO_2 of the umbilical venous blood is lower than that of the uterine veins. Placental metabolic consumption is incorporated as a reduction in the γ_{plac}. γ_{plac} is adjusted to calibrate umbilical vein SO_2.

4.6 Preferential streaming of umbilical venous return

In late gestation, approximately 20-30% of the oxygen rich blood coming from the umbilical vein passes through the ductus venosus and “preferentially streamed” to the left atrium across the foramen ovale [44]. In the model, we forced the oxygen concentration of the flow carried across FO to be equal to a mixture of IVC and DV flows. According to E4.12, when the flow through

FO is less than DV flow, all of the FO flow is derived by the DV. If the FO flow is greater than DV flow, then all the DV flow still goes to LA and the remaining FO flow is derived by the IVC.

$$\text{if } Q_{FO} \le Q_{DV}$$
$$[O_2]_{FO} = \frac{Q_{FO}[O_2]_{DV}}{Q_{FO}}$$
$$\text{else} \qquad \text{(E4.12)}$$
$$[O_2]_{FO} = \frac{Q_{DV}[O_2]_{DV} + (Q_{FO} - Q_{DV})[O_2]_{IVC}}{Q_{FO}}$$

Chapter 5

Hemodynamic and respiratory LPM of the fetal circulation

5.1 Hemodynamic LPM of the fetal circulation

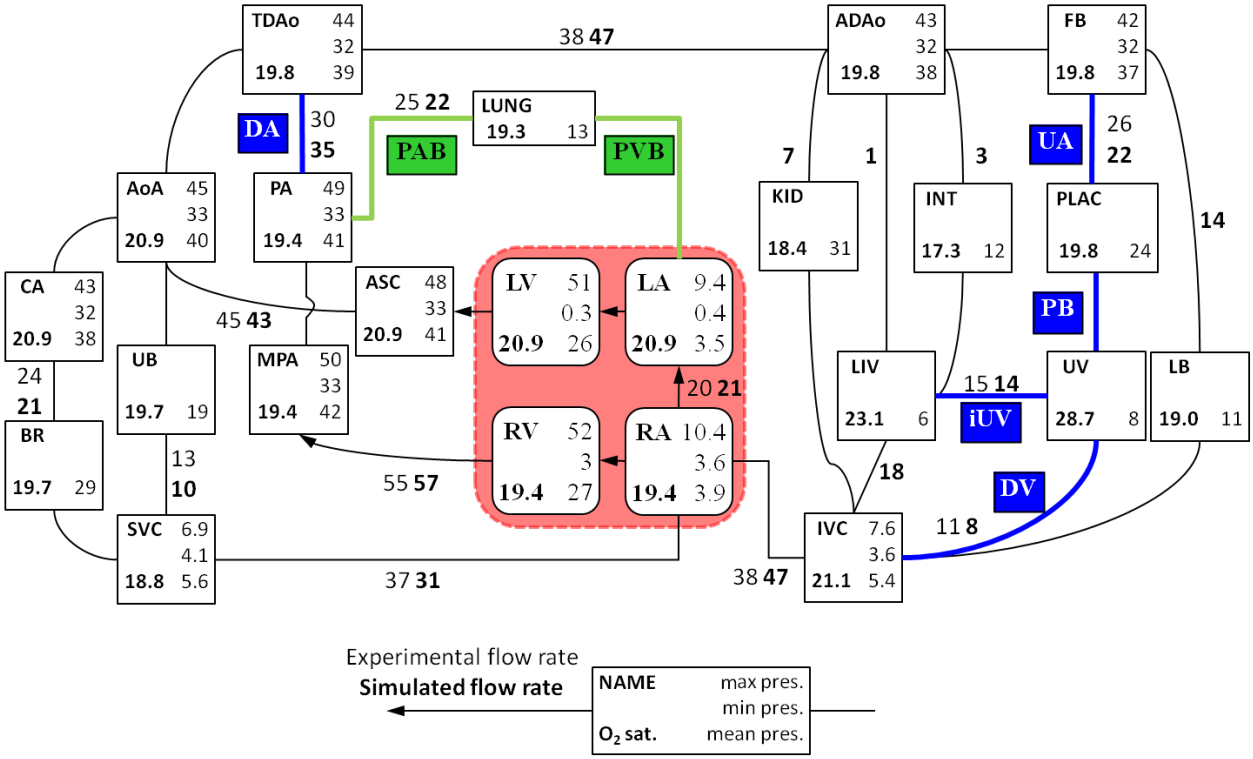

Figure 5.1 Network schematics of the transitionary fetal cardiovascular circuit. Connecting lines represent arterial, capillary and venous resistance elements, and compartments correspond to compliance chambers. Arrows describe the direction of trans-valvular flow. Cycle-averaged flow rate distributions as a percentage of combined cardiac output (% CCO) is labeled on the connecting vessels (CCO: 1.6 l/min), simulated flow rates are displayed in bold, experimental in vivo flow rates are selected values that are obtained from the literature [3, 45-48]. Minimum-maximum-mean pressures (mmHg), and oxygen saturations (%) as well as the names of the compartments are displayed in boxes. All values correspond to the fetal circulation just before birth at late-gestation period. *Blue* colored vessels represent the connections that close and *green* color represents connections that open during the fetal-to-neonatal transition. PAB: pulmonary arterial bed, PVB: pulmonary venous bed, UA: umbilical arteries, PB: placental bed and umbilical vein, iUV: intra-abdominal umbilical vein, DV: ductus venosus, DA: ductus arteriosus, LV: left ventricle, RV: right ventricle, LA: left atrium, RA: right atrium, ASC: ascending aorta, AoA: aortic arch, CA: carotid arteries, BR: brain, UB: upper body, TDAo: thoracic descending aorta, ADAo: abdominal descending aorta, KID: kidneys, LIV: liver, INT: intestines, FB: femoral bifurcation, PLAC: placenta, UV: umbilical vein, LB: lower body, IVC: inferior vena cava, SVC: superior vena cava, MPA: main pulmonary artery, PA: pulmonary arteries, LUNG: lungs. (CCO: combined cardiac output) Detailed nomenclature is provided in Table 1.

Using the neonatal and pediatric circulatory LPM framework developed by our group [18, 19, 22], we constructed a representative fetal circuit inspired from an earlier design by Pennati *et al*. [16]. Figure 5.1 shows the lumped parameter network of the fetal circulation, in which compliance chambers were used to model major vascular compartments, which were connected with linear resistance components. A nonlinear pressure-dependent model was used for the systemic arterial compliances [6, 11]. Nonlinear effects were left out for the venous and pulmonary arterial compliances.

Reference compliance and resistance values were adopted from Pennati *et al.* [16] and calibrated to match blood pressures and organ flow distributions of a near-term human fetus (~40 weeks, fetal weight=3500g) using clinical data [3, 38, 45-49].

During the cardiac cycle, arterial walls distend and stiffen under high pressure they become less distended and relaxed as the blood pressure decays. Stiffening of the arterial wall can be measured by comparing the change in arterial compliance between the lowest and maximum arterial pressures attained during a cycle. According to E3.4 this stiffening depends on the non-linear coefficient b of the pressure-dependent compliance and the change of pressure P during the cardiac cycle. For the systemic arteries, a value of -0.02 is chosen for b such that an approximate mean-to-systolic compliance ratio of 1.1-1.3 is calculated in the simulation, which agrees with the clinical observations [50, 51]. In order to determine the value of a (E3.3 and E3.4), we assumed that the value of linear compliance and the cycle-averaged value of the pressure-dependent compliance are very close. This assumption is backed up by findings in adult human that showed that the value of compliance calculated with these two methods (linear, non-linear) are approximately equal to each other [50]. Therefore, the value for the coefficient a is adjusted to obtain a cardiac-cycle averaged $C(P)$ to be equal to its reference linear compliance of the corresponding vessels [16, 50].

Numerical values for fetal LPM parameters are provided in Table 5.1 for compliance chambers, Table 5.2 for vascular resistance elements, Table 5.3 for the construction of the normalized time-varying elastance and volume intercept function (using to E2.9), and Table 5.4 for the construction of denormalized atrial/ventricular time-varying elastance functions (according to E2.7, E2.8, E2.10). Fetal and placental blood volumes were set to 276 ml and 164 ml, respectively [52].

Table 5.1 Compliance parameters of the fetal LPM

Parameter	Value		Parameter	Value
	a	*b*	C_{INT}	2.50E-04
$C_{ASC}^{\dagger}$	-5.60E-03	-0.02	C_{LB}	4.00E-03
$C_{AoA}^{\dagger}$	-8.80E-03	-0.02	C_{PLAC}	1.50E-03
$C_{TDAo}^{\dagger}$	-7.50E-03	-0.02	C_{BR}	3.00E-04
$C_{ADAo}^{\dagger}$	-4.30E-03	-0.02	C_{UV}	3.00E-04
$C_{FB}^{\dagger}$	-5.20E-03	-0.02	C_{SVC}	1.00E-03
$C_{CA}^{\dagger}$	-1.00E-03	-0.02	C_{IVC}	6.00E-04
C_{UB}	8.50E-04		C_{MPA}	8.00E-05
C_{KID}	2.00E-05		C_{PA}	8.00E-05
C_{LIV}	3.00E-03		C_{LUNG}	4.00E-04

C: compliance [L/mmHg]; ASC: ascending aorta, AoA: aortic arch, TDAo: thoracic descending aorta, ADAo: abdominal descending aorta, FB: femoral bifurcation, CA: carotid arteries, UB: upper body, KID: kidneys, LIV: liver, INT: intestines, LB: lower body, PLAC: placenta, BR: brain, UV: umbilical vein, SVC: superior vena cava, IVC: inferior vena cava, MPA: main pulmonary artery, PA: pulmonary arteries, LUNG: lungs,
†: values for *a* and *b* are shown according to Equation.5 for non-linear elements, otherwise linear compliance values are shown.

Table 5.2 Resistance parameters of the fetal LPM

Parameter	Value	Compartment	Parameter	Value	Compartment
R_{ASC}	2.0	ASC-AoA	R_{UVB}	81.7	UB-SVC
R_{AoA}	6.67	AoA-TDAo	R_{RVB}	233.3	KID-IVC
R_{TDAo}	0.67	TDAo-ADAo	R_{HV}	2.67	LIV-IVC
R_{ADAo}	1.0	ADAo-FB	R_{LVB}	25.0	LB-IVC
R_{CA}	5.0	AoA-CA	R_{DV}	21.7	UV-IVC
R_{UAB}	133.3	AoA-UB	R_{SVC}	3.33	SVC-RA
R_{RAB}	58.3	ADAo-KID	R_{IVC}	2.0	IVC-RA
R_{HAB}	1350	ADAo-LIV	R_{PA}	1.17	MPA-PA
R_{IAB}	566.7	ADAo-INT	R_{PAB}	81.0	PA-LUNG
R_{LAB}	116.7	FB-LB	R_{PVB}	26.7	LUNG-LA
R_{UA}	39.0	FB-PLAC	R_{DA}	5.0	PA-TDAo
R_{CAB}	25.0	CA-BR	R_{FO}	1.33	RA→LA
R_{HPV}	116.7	INT-LIV	R_{Ao}	1.33	LV→ASC
R_{PB}	45.3	PLAC-UV	R_{Mi}	1.33	LA→LV
R_{iUV}	8.3	UV-LIV	R_{Tr}	1.33	RA→RV
R_{CVB}	70.8	BR-SVC	R_{Pu}	1.33	RV→MPA

R: resistance [mmHg.min/L]; ASC: ascending aorta, AoA: aortic arch, TDAo: thoracic descending aorta, ADAo: abdominal descending aorta, FB: femoral bifurcation, CA: carotid arteries, UB: upper body, KID: kidneys, LIV: liver, INT: intestines, LB: lower body, PLA: placenta, BR: brain, UV: umbilical vein, SVC: superior vena cava, IVC: inferior vena cava, MPA: main pulmonary artery, PA: pulmonary arteries, LUNG: lungs, UAB: upper arterial bed, RAB: renal arterial bed, HAB: hepatic arterial bed, IAB: intestinal arterial bed, LAB: lower arterial bed, UA: umbilical arteries, CAB: cerebral arterial bed, HPV: hepatic portal vein, PB: placental bed, iUV: intra-abdominal umbilical vein, CVB: cerebral venous bed, UVB: upper venous bed, RVB: renal venous bed, HV: hepatic vein, LVB: lower venous bed, DV: ductus venosus, RA: right atrium, MPA: main pulmonary artery, PA: pulmonary arteries, PAB: pulmonary arterial bed, PVB: pulmonary venous bed, LA: left atrium, DA: ductus arteriosus, FO: foramen ovale, Ao: aortic valve, Mi: mitral valve, Tr: tricuspid valve, Pu: pulmonary valve; (see Figure. 1). Valves are unidirectional resistances with their directions indicated by (→).

Table 5.3 Coefficients used in E2.9 for the construction of isochrones models of ventricles

	$C^*(t)$		$V_0^*(t)$	
Index n	a_n	b_n	a_n	b_n
0	4.9040E-01	-	6.6564E-01	--
1	3.4058E-01	-2.6078E-01	-3.3050E-02	-4.2675E-01
2	-1.5423E-01	-1.0246E-01	1.2014E-01	-1.2889E-01
3	1.0990E-03	1.5528E-02	5.8652E-02	-5.6823E-02
4	5.0251E-03	-3.9879E-02	9.0261E-02	-2.0718E-02
5	4.3639E-03	-4.2478E-02	3.8926E-02	2.1415E-02
6	3.7844E-03	-7.8481E-03	3.0397E-02	6.0750E-03
7	9.3940E-03	-8.2504E-03	2.1130E-02	2.7220E-02
8	1.6743E-02	-5.6670E-03	3.3171E-03	1.6879E-02
9	7.4288E-03	-8.9272E-03	2.9544E-03	1.5218E-02
10	7.5099E-03	-3.8300E-03	-8.5289E-03	9.5840E-03
11	5.3551E-03	1.0485E-03	-5.0263E-03	1.6918E-03
12	4.4526E-03	4.7561E-04	-4.0416E-03	6.9291E-04
13	1.1452E-03	7.2932E-04	-2.1712E-03	-1.3402E-03
14	8.4064E-06	2.5297E-03	-1.5124E-03	-1.0808E-03
15	2.4719E-04	2.4930E-03	-1.3167E-04	-2.2124E-03

C*(t):normalized time varying compliance (l/mmHg), V_0(t): normalized time varying volume intercept (l)

Table 5.4 Atrial/ventricular elastance model parameters for the fetal LPM

Comp.	C_S	C_D	τ_S (min)	τ_D (min)	Comp.	ΔC	ΔV_0	C_{offset}	$V_{0,offset}$
LA	2.40E-02	6.00E-05	2.5E-03	7.5E-04	LV	6.67E-04	1.77E-02	5.65E-05	-1.34E-02
RA	0.80E-02	6.00E-05	2.5E-03	5.5E-04	RV	1.11E-03	2.94E-02	9.37E-05	-2.22E-02
Heart Rate		140 bpm	T_S/T	1/3					
T		0.0071 min	φ	0.41T					

C: compliance [L/mmHg]; V_0: volume intercept [L]; τ: time constant [min]; RA: right atrium, LA: left atrium, RV: right ventricle, LV: left ventricle; T: cycle duration; T_S: systolic duration of the cardiac cycle; φ: duration from the ventricular contraction to atrial contraction; S: systolic, D: diastolic,

5.2 Validation of the hemodynamic LPM

To ensure the validity of our fetal model, the following numerically predicted hemodynamic parameters: (i) combined cardiac output (CCO) and organ flow distribution, and (ii) arterial and umbilical blood pressures, were compared with the clinical measurements obtained from healthy term infants and from term fetal lamb when necessary.

Table 5.5 Summary of the central and organ flow distribution, and combined cardiac output data gathered from clinical measurements, and simulated by the model for the term human fetus.

Flow Distribution (%CCO)	Rudolph, 2009	Mielke, 2001	Rasanen, 1996	Kiserud, 2006	Molina, 2008	Pennati, 1999	Fetal Model
					44	**44**	**43**
LVO	**45**	**41**	**40**				
RVO	**55**	**59**	**60**		**56**	**56**	**57**
Pulmonary	**25**		**21**			**17**	**22**
Placental	**26**			**21**		**20**	**22**
DA	**30**	**46**	**31**			**44**	**36**
FO	**20**	**33**	**19**			**27**	**21**
Brain	**24**					**13**	**21**
Upper Body	**13**					**12**	**10**
Renal						**10**	**7**
Intestines						**4**	**3**
Lower Body	**12**					**24**	**14**
Hepatic Vein	**14**					**19**	**18**
DV	**11**					**19**	**8**
SVC	**37**					**26**	**31**
IVC	**38**					**57**	**47**
CCO (ml/min)	**1575**	**1488**	**1900**	**1400**	**651**	**1452**	**1600**

CCO: combined cardiac output, LVO: left ventricular output, RVO: right ventricular output, DA: ductus arteriosus, FO: foramen ovale, DV: ductus venosus, SVC: superior vena cava, IVC: inferior vena cava. Flow distribution is expressed in terms of percentage of the combined cardiac output. Combined cardiac output is the sum of left and right ventricular outputs.

As stated in literature [3], clinical reports on *in utero* flow measurements show a large variability. For this reason, we selected two main reviews on fetal circulation by Rudolph [3] and

Kiserud [1] to obtain reference values for CCO and organ-level flow distribution for the fetus. Original data can be viewed from respective publications [45-48], and selected values for organ flow distributions are displayed in Figure 5.1 and Table 5.5 for direct comparison. Simulated fetal CCO was 1600 ml/min, which is in accordance with the reported CCO for term-fetus (ranging from 1400-1900 ml/min in Doppler echocardiography [48] and ultrasound [45, 46], 651 ml/min in recent 4-D ultrasound investigations [47]). The largest disparity in flow distribution between the model and measurements was 28% in hepatic vein, followed by DV (27%) and inferior vena cava (IVC) (24%), which are in the standard subject-subject deviation.

Due to the lack of clinical data owing to the practical difficulty of pressure measurements *in utero*, LPM pressures were mainly validated during the neonatal period for which clinical data exist [38, 49] (covered in Chapter 6). Umbilical cord pressure measurements during cordocentesis in normal fetuses showed that umbilical venous pressure was 6.5 mmHg on the average [53]. Simulated umbilical venous pressure (P_{UV}) was 8 mmHg. In the ascending aorta (ASC in Figure 5.1) maximum pressure during a cycle was 59 mmHg during systole, minimum pressure was 32 mmHg during diastole, and the mean pressure was calculated as 42 mmHg. In the main pulmonary artery (MPA in Figure 5.1) maximum pressure was 61 mmHg during systole, minimum pressure was 32 mmHg during diastole, and the mean pressure was calculated as 44 mmHg. Arterial pressure measurements in fetal sheep are varied in the literature. In fetal lamb, reported systolic/diastolic pressures were 70/45 mmHg in [54], on the other hand reported mean pressures [55] were 45±5.7mmHg in brachiocephalic arteries (38 mmHg in our model), 47.8±6.0 mmHg for the pulmonary arteries (41 mmHg in our model), 42.9±1.8 mmHg for the abdominal aorta (38 mmHg in our model), 2.4±0.6 mmHg and 2.9±1.0 mmHg in the right and

left atrium (3.9 and 3.5 mmHg in our model), respectively. Simulated pressures are generally 1SD lower than the measured fetal lamb pressures.

5.3 Respiratory model of the fetal circulation and its validation

A pulmonary gas exchange model based on lumped alveolar-capillary gas diffusion mechanics [23, 56] was modified to simulate the placental gas exchange. Details and modeling assumptions regarding the gas exchange component are presented fully in Chapter 4. Table 5.6 shows the parameters used in the placental respiration model.

Table 5.6 Parameters of placental respiration

Parameter	Description	Placental
$[O_2]_I$	Inspired O2 concentration	$= H_M^{-1}(100 \text{ mmHg})$
r	Ventilation-Perfusion Ratio	$= \frac{600 \text{ ml/min}}{Q_{plac}}$
γ	Diffusion efficiency of respiratory membrane	0.45

Table 5.7 shows the organ level metabolic consumption that is distributed such as to match oxygen saturation levels obtained from fetal lambs, although metabolic differences between human and lamb were taken into account [3]. Total oxygen consumption of the human fetus corresponds to 25-32 ml/min for a 3.5 kg fetus, excluding the oxygen consumption of the placenta [3].

Table 5.7 Organ flow distribution and metabolic rates in fetal lamb and in fetal LPM

	In utero Lamb[3]		Fetal LPM	
Organ	%CCO	Metabolic Rate Percent of Total	%CCO	Metabolic Rate Percent of Total
Upper+Lower Muscle, Skin, Bone	29.4	40	24	35
Heart	3.3	12	-	-
Brain	4.2	12	21	31
Kidney	2.9	4	7	6
Liver	25.2	23	18	18
Intestines	5.2	5	3	5
Lungs	5.2	4	22	5
Placenta	39.4	-	22	-
Total Metabolic Rate (mlO_2/min)		26.4		26.6

Organ level S_{O2} distribution is presented in Figure 5.1. For the validation of gas exchange parameters, simulated O_2 concentration data were compared to umbilical cord O_2 measurements in the fetus and newborn [3, 57]. According to the lamb studies [3], *in utero* umbilical vein (UV) oxygen saturations ($S_{O2\text{-}UV}$) are about 80–85%, and umbilical arterial oxygen saturations ($S_{O2\text{-}UA}$) are about 50%. Similarly, umbilical cord blood samples obtained after birth from human placenta had an average PO_2 of 28.3 mmHg at the UV (SD: ±6.7, $S_{O2\text{-}UV}$: 64.4±15.1%) and 15.7 mmHg UA (SD: ±5.3, $S_{O2\text{-}UA}$: 25.8±15.4%) for term infants of normal birth weights [57]. Placental respiration efficiency parameter was calibrated (γ_{plac} = 0.45) until we achieved 19.7 mmHg at the fetal UA ($S_{O2\text{-}UA}$: 49.2%) and 28.7 mmHg at the fetal UV ($S_{O2\text{-}UV}$: 72.1%) (see Figure.5.1).

Chapter 6

The effect of umbilical cord clamping on the hemodynamics and gas exchange during the transition from fetal to neonatal circulation

6.1 Introduction

Circulatory physiology of the newborn goes through complex transitions in order to shift the respiratory function from the placenta to the lungs, that is characterized by the closure of fetal shunts, expansion of lungs, and removal of placental circulation [4, 58]. During the natural course of birth, umbilical arteries (UA) slowly close under the effect of increased oxygen tension [59, 60] and vasoconstrictors secreted by newly functioning lungs [61]. However, in order to speed up and to manage the fetal-to-neonatal transition, immediate cord clamping (ICC), has been adopted as a standard clinical practice. ICC is employed over more than 50 years, but has recently been challenged, as it is hypothesized that the sustained umbilical flow at birth achieved through delayed cord clamping (DCC) can be beneficial for the neonate [62, 63]. Systematic reviews of DCC in term and preterm infants results in increased blood volume [52, 64-66], reduced need for blood transfusion [62], decreased incidence of intraventricular hemorrhage [62], and decreased frequency of iron deficiency anemia [67, 68]. Conversely, DCC results in an increase in neonatal jaundice requiring phototherapy. These findings have recently led to the American Congress of Obstetricians and Gynecologists (ACOG) recommendation that delayed cord clamping for 30-60 seconds should be performed for all preterm infants [69], yet a consensus is not established for term infants and infants requiring resuscitation [70]. Recent *in vivo* observations provided supportive evidence on the adverse effects of ICC on the cardiovascular function in preterm infants. Comparative studies in preterm lambs [71] and preterm infants [72] showed that DCC improves cardiovascular function through improved hemodynamic stability, increased cardiac output (CO) during and following the immediate transition from placental to pulmonary

respiration [71], and increased superior vena cava (SVC) return and improved right ventricular output (RVO) over the critical first days of life [72]. These observations, strengthen the view that the reduced cardiovascular function in ICC can be associated with neonatal hypovolemia [63]. In the absence of placental transfusion, blood volume that fills the expanding pulmonary vasculature needs to be drawn from the venous bed, leaving the infant hypovolaemic.

Comparative quantitative studies of ICC and DCC that focus on premature infants are limited in the literature [71, 72]. Further, the cardiovascular mechanisms relating hemodynamics to placental transfusion and hypovolemia, as well as the effect of cord clamping on respiratory gas levels are not clearly identified. Our aim in this study is to 1) construct a physiologically accurate and detailed model of the transition from fetal to neonatal circulation at birth, 2) investigate and compare the two cord clamping scenarios, namely DCC and ICC, based on their relative impacts on the hemodynamics, and respiration in the transitioning circulation of a term infant.

In order to provide a "quantitative" understanding of the complex series of hemodynamic events during cord clamping, we developed a numerical lumped parameter model (LPM) of the fetal circulation simulating the late gestation-to-neonatal transition period for human. Existing knowledge of fetal circulation and specifically its transitional events are mostly based on animal studies [3, 54, 71, 73-76]. *System-level* hemodynamic investigation of *continuous* transition from fetal-to-neonatal circulation in human has not been undertaken to our knowledge except for a simplified representation without gas exchange, whilst isolated lumped parameter studies of fetal circulation at late gestation are available in literature [16, 17, 24, 29].

In this study, in order to simulate the oxygen levels in the blood during the fetal transitional events, a placental and a pulmonary gas exchange module is coupled with the LPM. O_2 and CO_2 gas exchange is incorporated through a detailed respiratory model to compare the

effect of cord clamping procedures on the organ-level oxygen saturations at birth. Prediction of fundamental vasoactive gases in relation to the cord clamping procedures is essential as placental flow is associated with the expansion of the lung vasculature [63]. If the placental return is removed prematurely, an important pulmonary vasodilator function is lost. Moreover, placental blood contains important cues for vasoactive remodeling, such as prostaglandins PGE_2 [4, 77]. Although these help conserve the fetal status of the pulmonary vasculature and the shunts *in utero,* their exact function in transition from fetal to neonate is unknown [4, 78]. Therefore, ICC has the likelihood of altering fetal transition through multiple pathways where the hemodynamic and respiratory components can be dissected with the present parametric numerical study. Likewise, there has been an ongoing need for quantitative information of the early neonatal circulation and the effects of cord clamping in the human, particularly for new management options for neonatal resuscitation [70] and associated device options [63]. We believe present model would be important for neonatologist in understanding fetal transition in detail and improve clinical interventions with the transitioning fetal circulation.

The present chapter is organized as follows; in the Section 6.2, the computational model is described for transitional hemodynamics and gas exchange. In the Section 6.3, the details of validation, and the results for hemodynamics and gas transition in ICC and DCC are presented. In the Section 6.4, we analyze and compare the potential benefits of DCC over ICC on the hemodynamics, cardiac function, physiologic stability and, and O_2 saturations. We also discuss present potential mechanisms for vasoactive remodeling processes involved in DCC and provided explanations for the major clinical observations through our results.

6.2 Methodology

6.2.1 Transitional fetal shunts:

Transition from the fetal-to-neonatal circuit is modeled by prescribing time-varying resistance functions for the UA, placental bed (PB), intra-abdominal umbilical vein (iUV), ductus venosus (DV), ductus arteriosus (DA), pulmonary arterial bed (PAB) and pulmonary venous bed (PVB) (transitioning vessels are shown explicitly in Figure 5.1).

The duration of the fetal transition is governed by a constant, τ, which defines the amount of time for the resistance to reach its neonatal value. We found that transitional dynamic changes in the pulmonary and DA flow [76], pulmonary and aortic pressure [38], and pulmonary flow and pressure [4] are best reflected when relating the resistance (R) transition to a logarithmic conductance change in the pulmonary vascular bed (PAB+PVB), and to a linear change in the effective vessel diameter (d_{eq}) of the DA using the Poiseuille law that relates the diameter to the resistance of a conduit, i.e. $R(t) \sim \frac{1}{d_{eq}(t)^4}$ [79]. **(E6.1)** describes the resistance remodeling in the DA, DV, UA, PB and iUV where t0 is the time point of the beginning of the transition, resistance values of the specified vessels transitions are altered starting from its initial value of R_0 until it reaches R_f at the end of the transition. UA (in DCC) and DV transition were simulated similar to DA.

$$R_{DA,DV,UA,PB,iUV}(t) = \frac{R_0 R_F \tau^4}{\left((t-t_0)R_0^{1/4} + (t_0+\tau-t)R_f^{1/4}\right)^4} \quad \text{(E6.1)}$$

Neonatal state resistances of the PAB and PVB were calibrated to match the simulated pulmonary arterial pressure with clinical measurements made at the same site during the 10th to 40th hours of life [38, 49]. A logarithmic conductance change function is found suitable to simulate pulmonary vascular resistance (PVR) transition **(E6.2)**, which is characterized by an

initial rapid decline in the first 24 hours followed with a gradual decrease over the next 2 days [38]. PVR transition function parameters were calibrated to match physiologic measurement of PVR in fetal sheep at birth [76] (R^2=0.97). In E6.2, Q ensures that $R=R_0$ when $t=t_0$. β is the growth rate and set to achieve $R = \left((1-\gamma)R_0^{-1} + \gamma R_f^{-1}\right)^{-1}$ at $t=t_0+b.\tau$ (γ=0.5, b=0.1).

$$\begin{cases} R_{PAB,PVB}(t) = \dfrac{R_F}{1 + Qe^{\beta\frac{t-t_0}{\tau}}} \\ \beta = \dfrac{\ln(1-\gamma)}{b} \\ Q = \left[\dfrac{R_F}{R_0} - 1\right] \end{cases} \quad \text{(E6.2)}$$

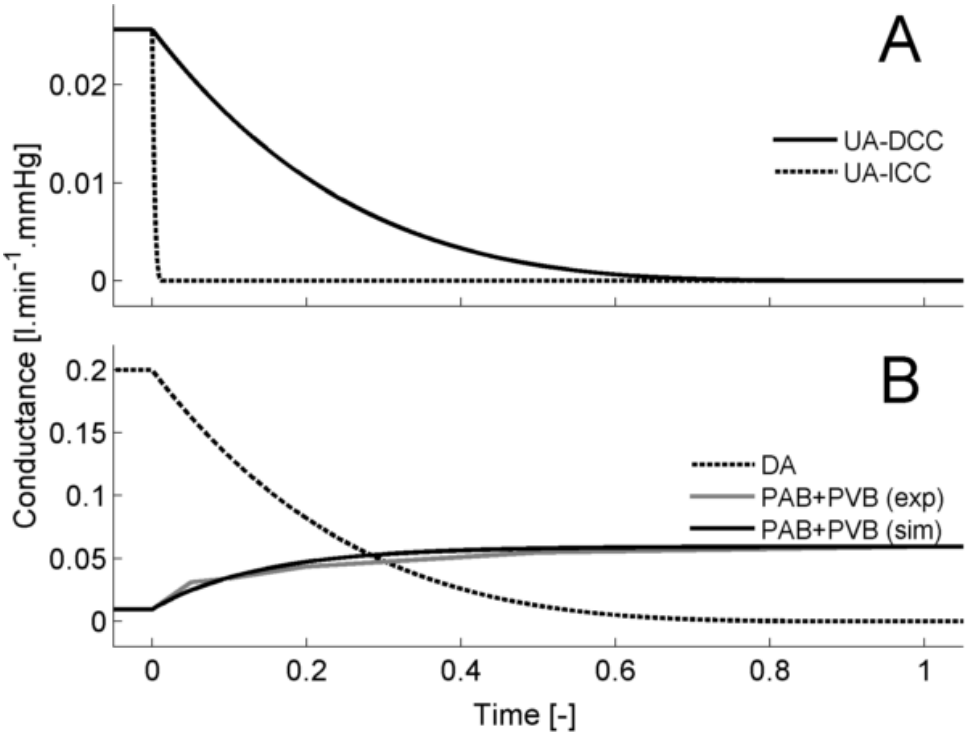

Figure 6.1 Vascular conductance changes of selected vessels during the transition period. A: Umbilical artery (UA) constriction in ICC (*dashed lines*) and DCC (*solid lines*). B: Conductance history of the ductus arteriosus (DA, *dashed*) and pulmonary vascular bed (PAB+PVB, *continuous*) during the transition period. Gray solid line shows the experimentally obtained curves [76], black solid lines represent simulated trend. Complete transition of all vessels were defined to complete at time = τ, which is 10 minutes in our simulation. Time is normalized to the τ. (DCC: delayed cord clamping, ICC: immediate cord clamping)

In order to model ICC, we set the UA and PB resistances to shut immediately at the onset of the transition. In the case of DCC, UA resistance was slowly shut (τ=10 minutes), while PB and iUV resistance remained open to allow placental transfusion. Otherwise, all shunts (including pulmonary circulation) were assigned a τ of 10 minutes. Figure 6.1A depicts the time dependent closure of UA in the ICC and DCC scenarios, and Figure 6.1B shows the simulated resistance remodeling in DA and pulmonary vascular bed (PAB+PVB) compared with the experimentally measured PVR curve (scaled to initial and final values of PVR in the model). Neonatal resistance values are shown in Table 6.1.

Table 6.1 Neonatal resistances (only parameter that are different than fetal state are shown)

Parameter	Value (ICC)	Value (DCC)	Compartment
R_{PAB}	10.1	10.1	PA-LUNG
R_{PVB}	6.67	6.67	LUNG-LA
R_{DA}	inf	Inf	PA-TDAo
R_{DV}	inf	Inf	UV-IVC
R_{iUV}	inf	8.33	UV-LIV
R_{PB}	inf	45.3	PLAC-UV

ICC: immediate cord clamping, DCC: delayed cord clamping; R: resistance [mmHg.min/L]; PAB: pulmonary arterial bed, PA: pulmonary arteries, LUNG: lungs PVB: pulmonary venous bed, LA: left atrium, DA: ductus arteriosus, TDAo: thoracic descending aorta, DV: ductus venosus, UV: umbilical vein, IVC: inferior vena cava, iUV: intra-abdominal umbilical vein, LIV: liver, PB: placental bed, PLAC: placenta; see (Figure.1)

Clinically observed placental transfusion when cord is clamped at 2 minutes after birth is around 50 ml [80]. In order to match this value in the simulation, 28 ml of placental unstressed blood volume is converted to stressed blood volume (descriptions for stressed and unstressed blood volumes can be viewed in Chapter 3 Section 1) in the first 0.5τ with a sigmoid function. This behavior represents the *in vivo* placental vascular contractions [81].

All other parameters, including the heart rate and compliances, were kept constant through the fetal and neonatal models, therefore excluding the potential effects of bradycardia from our model.

6.2.2 Transition – Gas Exchange:

Gas exchange in the placenta continues throughout the transition in both clamping scenarios. However, oxygen extraction from the placenta terminates as soon as fetal placental flow becomes zero, consequently ending abruptly in the ICC case.

Table 6.2 Parameters of pulmonary respiration during the transition

Parameter	Description	Pulmonary
$[O_2]_I$	Inspired O2 concentration	$= \frac{150 \text{ mmHg}}{RT}$
r	Ventilation-Perfusion Ratio	$r = \begin{cases} 0 & if\ t < t_0 \\ 0.7\frac{t - t_0}{\tau} & if\ t_0 < t < t_0 + \tau \\ 0.7 & if\ t > t_0 + \tau \end{cases}$
γ	Diffusion efficiency of respiratory membrane	1

In Table 6.2 showing the parameters of pulmonary respiration, representing the non-breathing neonate, V/Q at the lungs is initially set to zero at the moment of birth, and increases until it reaches the value observed in newborns at 24 hours after birth (V/Q=0.63±0.7) [82], at the end of the 10 minutes of pulmonary expansion. Owing to the lack of clinical data, we assumed a linear relation between time and the value of V/Q, therefore findings are of comparative value. Nevertheless, our results showed a good agreement with the *in vivo* measurements on infants with ICC and DCC (see Section 6.3.3 – Gas Exchange). Fetus and placenta were assumed to stay leveled on the same height and the effect of gravity was neglected [80]. Heart rate was kept constant at 140 beats per minute [45], through the entire simulation.

6.3 Results

6.3.1 Validation of the Fetal-to-Neonatal Transition: flow and pressures

To ensure the validity of our model, the following numerically predicted hemodynamic parameters; (i) combined cardiac output (CCO) and organ flow distribution, (ii) arterial and umbilical blood pressures, and (iii) dynamic flow-pressure patterns were compared with the clinical measurements obtained from healthy term infants before and after birth. Validation of the fetal circulation is already presented in Chapter 5.

Table 6.3 Summary of the simulated and clinical pressure data for the fetal human-lamb, and for the human newborn.

Pressures (mmHg)	Human Fetal	Lamb Fetal	Human Newborn				Model Results		
	Ville, 1994	**Iwamoto, 1987**	**Emmanouilides, 1964**		**Kitterman, 1969**		**Fetal**	**Neonatal w/ ICC**	**Neonatal w/DCC**
			1-10 hour	**>40 hours**	**1 hour**	**12 hours**			
Systemic		70/45	75/36 (45)	71/49 (59)	70/44 (53)	66/41 (50)	59/32 (42)	75/36 (48)	94/45 (60)
Pulmonary		70/45	56/27 (34)	40/12 (25)			61/32 (44)	44/11 (22)	55/13 (28)
Umbilical Vein	(6)						(6.5)		

Systemic and pulmonary pressure measurements for the newborn were available until the 1st hour of postnatal life up to 50 hours. Simulated results are presented for the fetal state, and the end-transition states after immediate cord clamping (ICC) and delayed cord clamping (DCC). Values are Systolic/Diastolic (Average) pressure.

Table 6.3 presents a comparative display of modeled and clinically measured fetal/neonatal blood pressures. Due to the scarcity of *in utero* pressure measurements, validation of pressures was restricted only to the neonatal stage. For the validation of neonatal circulation, systemic and pulmonary arterial pressures were sampled at the ascending aorta and the main pulmonary artery chambers (ASC and MPA in Figure 5.1.1). Results from the simulation proved

good match with pressure measurements obtained *in vivo* at 10th to 48th hour of life [38, 49] (after the closure of fetal shunts). In the simulation of the ICC case, neonatal state systolic/diastolic pressures sampled at ASC were 64/39 mmHg, and the mean pressure was calculated to be 51mmHg (compared to 71/49 (59) mmHg *in vivo*), whereas at the pulmonary side systolic/diastolic pressures were computed to be 40/17 mmHg, with a mean pressure of 28 mmHg (compared to 40/12 (25) mmHg *in vivo*). Pulse pressures were slightly lower in the simulation compared to *in vivo*; however, this is still in the acceptable range, and do not affect our conclusions.

6.3.2 Dynamic flow patterns during the transition in immediate and delayed cord clamping

6.3.2.1 Umbilical cord flow and placental transfusion

Placental transfusion relies on the asymmetric constriction of the umbilical vessels, where umbilical arteries constrict and umbilical vein remains patent if the cord clamping is delayed during its natural course. With the cessation of umbilical arterial flow, placental volume shift is driven by the positive pressure gradient from the placental bed towards IVC ($\Delta P_{PLAC-IVC}$=18 mmHg at t=0).

Knowing the order of magnitude of the placental transfusion rate can help clinicians in determining the timing of the cord clamping for achieving a desired transfusion volume. Figure 6.2A depicts a quasi-linear volume shift from the placenta, 90% of transfusion was achieved at 5th minute (t=0.5τ), and beyond the 8 minutes mark there was practically no further increase in the fetal blood volume. Figure 6.2B shows that the decaying flow through the umbilical vein lasted until 0.8 τ, whereas it ceased immediately in ICC. In DCC, the placental transfusion volume amounted to 53.3 ml, which increased neonatal blood volume by 19.3%; meanwhile

circulating stressed blood volume increase was 34%. As such, circulating stressed blood volume is the portion of blood volume which contributes to the generation of baseline venous pressure and it is an important factor in ventricular filling [83] (a detailed description is given in Chapter 3). As explained in Sections 6.3.2.3 and 6.3.2.4 in this chapter, placental transfusion marked the major long-term effects of DCC by improving CO through an increased preload.

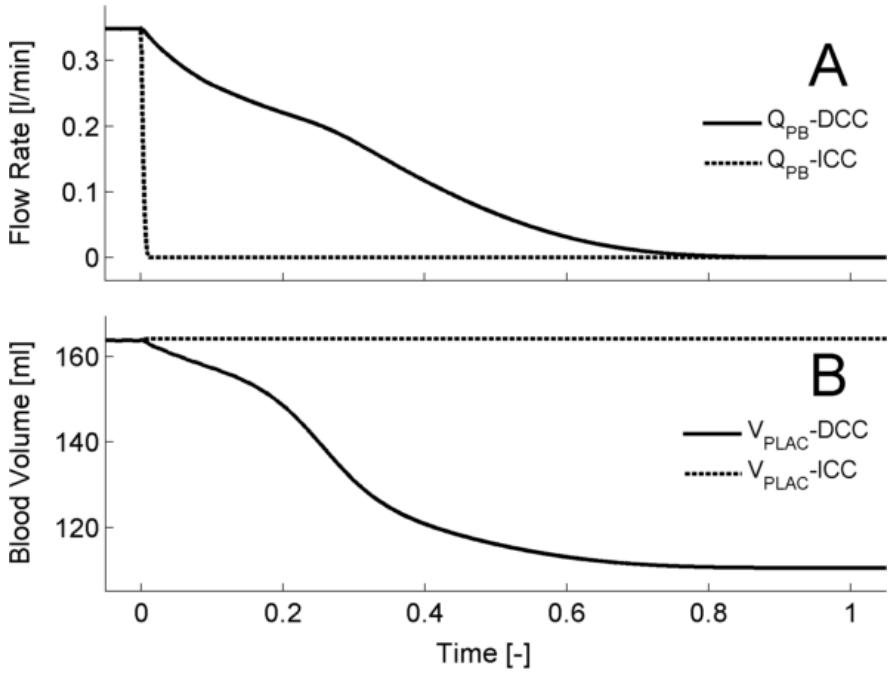

Figure 6.2 Dynamics of blood volume shift from the placental bed to the fetus that occurs during the transition, computed as a function of time. A: Cardiac-cycle averaged flow rate in the placental bed (Q_{PB}), with DCC and ICC. In the ICC case, Q_{PB} ceased immediately. In DCC, Q_{PB} decayed until 80% of the transition time has passed. B: Placental blood volume (V_{PLAC}) in milliliters, placental transfusion amounted to 53.3 mls in DCC. *Dashed* and *continuous* curves represent ICC and DCC, respectively. Complete transition of all vessels were defined to complete at time = τ, which is 10 minutes in our simulation. Time is normalized to the τ. (DCC: delayed cord clamping, ICC: immediate cord clamping)

6.3.2.2 Ductus Arteriosus and the pulmonary circulation

Independent of the cord clamping scenario, DA maintained a predominant right-to-left flow direction during the early stages of the transition, though it became a bidirectional shunt

immediately after. This trend is displayed in Figure 6.3A. Reversal of the flow is attributed to the reversed pressure gradient across DA, which resulted from a decreased PVR and a simultaneous increase in systemic vascular resistance (SVR) and left ventricular output (LVO), as presented in Figure 6.4. The DA flow direction was reversed to left-to-right at a point roughly around 10% through the transition (t=0.1τ), which occurred significantly earlier in the ICC (at t=0.07τ) compared to DCC (at t=0.12τ).

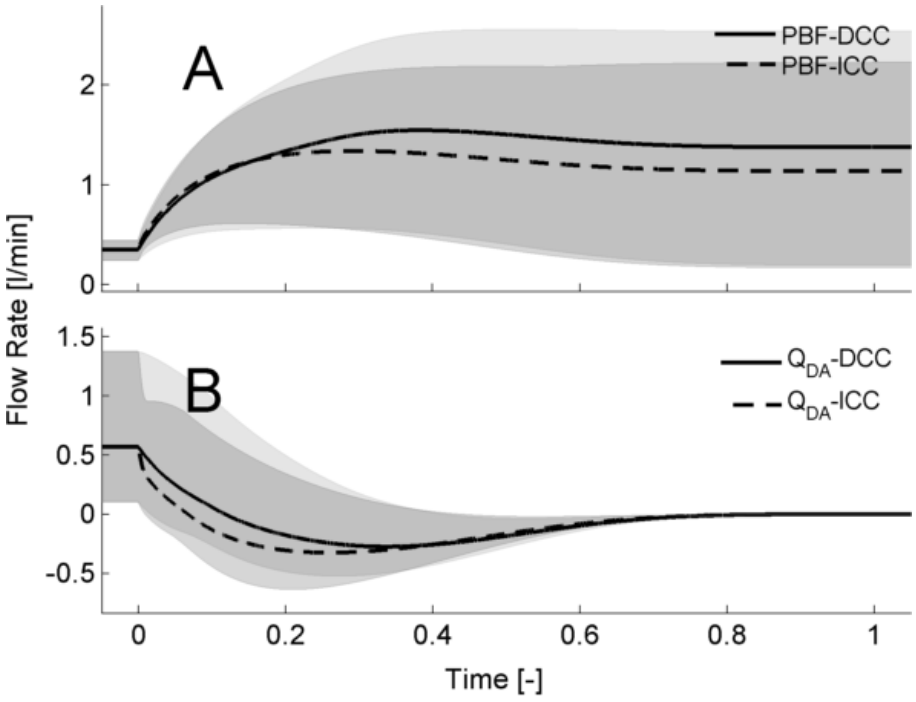

Figure 6.3 Effects on pulmonary perfusion. Comparison of the ductus arteriosus blood flow (Q_{DA}) and the pulmonary blood flow (PBF), during the transition. A: Cardiac-cycle averaged Q_{DA}, positive values indicate a right-to-left shunt. Predominant flow reversal occurs earlier in ICC compared to DCC (at time= 0.07τ vs. 0.12τ). For the rest of the transition, DA is primarily a left-to-right shunt. B: Cardiac-cycle averaged PBF increases rapidly with expanding lungs. DA reverse flow is the major contributor to the pulmonary flow shift during mid-transition. *Continuous* and *dashed* curves represent DCC and ICC cases, respectively. Shaded area represents the maximum and minimum pulsatile flow during a cardiac cycle, dark gray: ICC, light gray: DCC. Complete transition of all vessels were defined to complete at time = τ, which is 10 minutes in our simulation. Time is normalized to the τ. (DCC: delayed cord clamping, ICC: immediate cord clamping)

With the expansion of lungs, pulmonary blood flow (PBF) rapidly increased to 380% of its baseline fetal value where it peaked around 0.3τ in the ICC case (Fig. 6.3B) and with a delayed peak in DCC occurring at around 0.38τ. Following to that, PBF decreased in parallel with the constriction of DA, until it stabilized roughly at 1.38 l/min in DCC and 1.15 l/min in ICC with the closure of DA. PBF was noted to be higher in DCC than in ICC during the transition, and remained to be higher at the end of the transition.

Apparent relationship between the dynamic flow patterns in the PAB (PBF) and DA (Fig. 6.3A-B) indicates that DA reverse flow is the major contributor to the PBF overshoot during mid-transition. Simulated pulmonary and DA flows show realistic transition patterns similar to that was reported in animal experiments by Crossley *et al* [76].

6.3.2.3 Ventricular function

Functional trends of the ventricles are plotted in Figure 6.4. LVO and, more severely, RVO suffered a temporal drop immediately after cord clamping (ΔLVO_{drop}=20 ml/min, ΔRVO_{drop} =80 ml/min), associated with a decreased venous return and increased afterload caused by the sudden removal of the low resistance placental pathway. However, following to that RVO and LVO rapidly increased due to the decreased PVR.

Shortly after the initial establishment of pulmonary circulation, FO mediated LV filling was replaced with a greater pulmonary venous return, which was further enhanced by the reversed DA flow. Consequently, LVO benefited from a two-fold increase (1550 mls/min in DCC, 1334 mls/min in ICC) and exceeded RVO during the mid-transition. Capturing the previous descriptions of the changes in LVO in human newborns [84], closure of DA was largely responsible for the gradual decrease in PBF and LVO during the latter half of the transition.

Change in RVO was characterized by a rapid increase until the closure of FO, which then continued to increase slowly until the closure of DA. Besides differences in their magnitudes, transitional trends were similar for ventricular outputs in DCC and ICC.

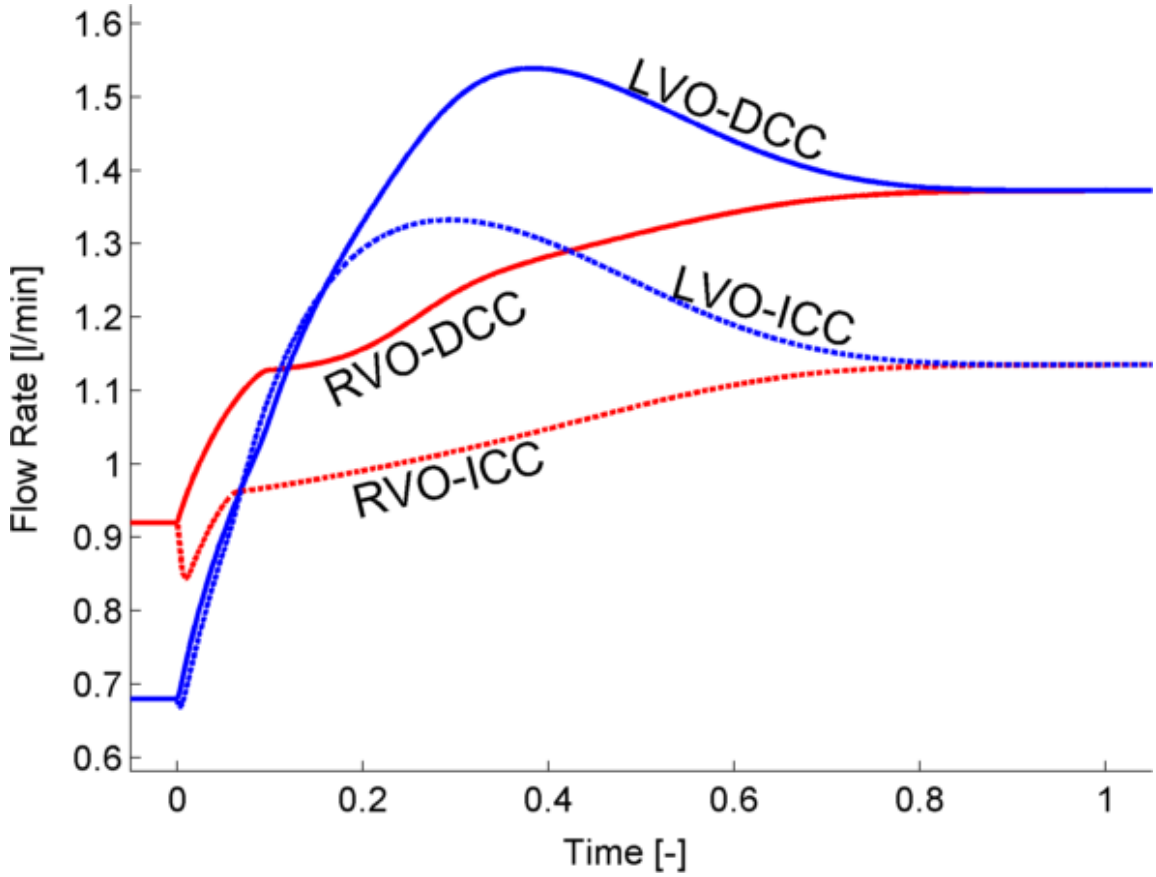

Figure 6.4 Mean ventricular function during fetal transition for DCC and ICC. Cardiac-cycle averaged left (*blue*) and right (*red*) ventricular outputs (LVO and RVO) during the transition. *Continuous* and *dashed* lines represent DCC and ICC cases, respectively. Complete transition of all vessels were defined to complete at time = τ, which is 10 minutes in our simulation. Time is normalized to the τ. (DCC: delayed cord clamping, ICC: immediate cord clamping)

At the end of the transition, the systemic and pulmonary circulations are separated and LVO and RVO equilibrated delivering a CO of 1135 ml/min in ICC and 1379 ml/min in DCC. Since the heart rate was kept constant throughout the simulation, this remarkable increase in CO with DCC (approximately by 20% compared to ICC) is solely attributed to an increased preload

which induced a higher stroke volume (SV) through the Frank-Starling mechanism, that is clearly visible in the pressure-volume (PV) curves of ventricles (Figure 6.3.5). Increased blood volume in DCC is reflected in a 32% and a 73% increase in pre-load pressures compared to ICC, in left and right ventricles, respectively.

6.3.2.4 Arterial Pressure and Ventricular Pressure-Volume Curves

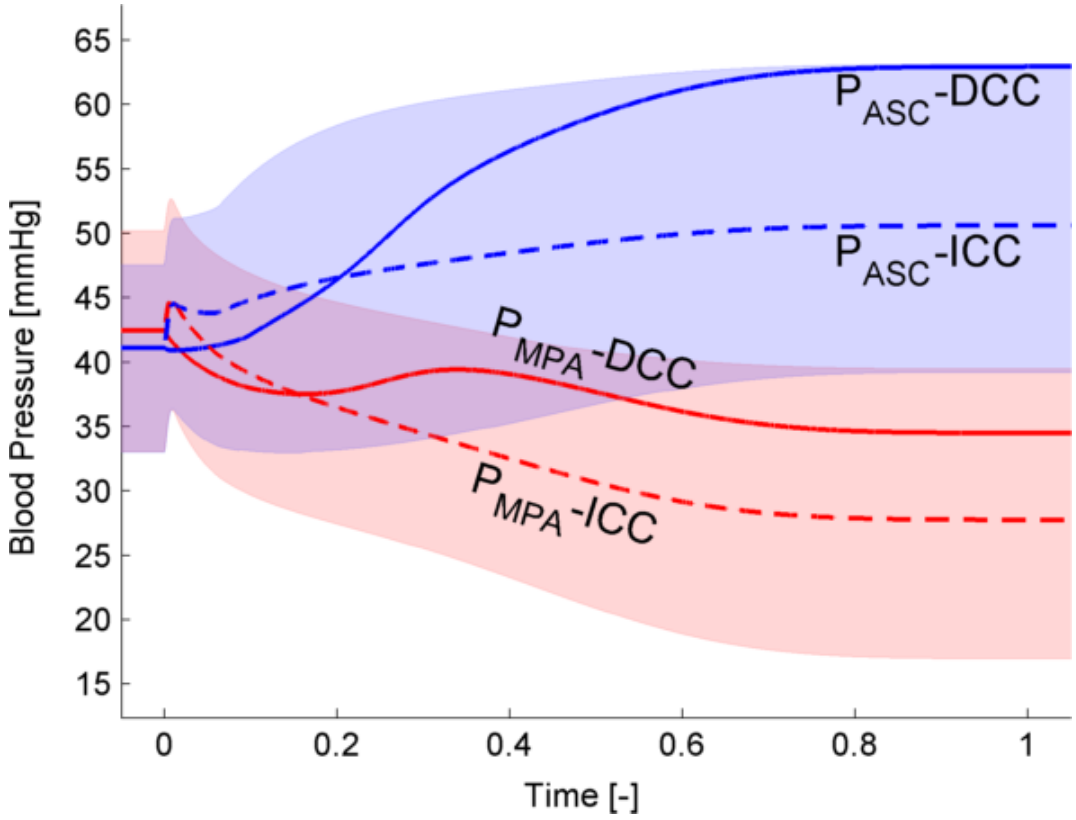

Figure 6.5 Mean arterial pressure changes during the transition for DCC (continuous lines) vs. ICC (dashed lines) in the Ascending Aorta (ASC, *blue*) and Main Pulmonary Artery (MPA, *red*). DCC blood pressures were higher during most of the transition period and remained to be higher at the end of the transition. ICC generated a pressure wave (which had a magnitude of 2.4 mmHg at the MPA, and 3.4 mmHg at the ASC) during the early transition period. Shaded area plotted only for ICC, represents the maximum and minimum pulsatile pressures during a cardiac cycle, blue shade: P_{ASC}, red shade: P_{MPA}. Complete transition of all vessels were defined to complete at time = τ, which is 10 minutes in our simulation. Time is normalized to the τ. (P: pressure, DCC: delayed cord clamping, ICC: immediate cord clamping)

Dynamic changes in arterial blood pressures are plotted in Figure 6.5. At the beginning of the transition, a pressure wave in systemic and pulmonary arteries (with a magnitude of 2.4 mmHg at the MPA and 3.4 mmHg at the ASC) is observed in the ICC due to the sudden increase in SVR. Pressure wave was also observed in carotid arteries and caused a sudden but transient increase in cerebral blood flow by 9.6%. Transition of pressures was smoother in the DCC case, although changes in the magnitude were greater. Overall, DCC favored higher arterial blood pressures compared to ICC by 23.5%, with 87/48 (63) mmHg at the ASC, and 46/22 (34) mmHg at the MPA in DCC. The primary reason behind the higher mean blood pressures in DCC was the increase in CO and partly the increased blood volume.

Ventricular PV curves are presented in Figure 6.6. Fetal ejection fractions were 60% for LV and 53% for RV, being in the range of clinical measurements albeit lower than the average (72.2% and 62.4%, respectively for LV and RV) [37]. In both clamping cases, afterload was increasing for the LV, and decreasing for the RV. In DCC, end-diastolic volume of the RV increased from 12.3 ml to 14.9ml, whereas in the ICC it reduced to 10.9 ml. Increase in RV SV was attributed primarily to an increased ejection fraction (DCC: 66%, ICC: 75%). In the LV, both ejection fraction (DCC: 63% ICC: 65%) and end-diastolic volume (Fetal: 8 ml, DCC: 15.6 ml, ICC: 12.6 ml) contributed to the increase in SV.

At the end of the transition, total stroke volume of the heart is increased compared to the fetal state (SV_{fetal}= 11.4 ml), in both ICC ($SV_{T,\ ICC}$= 16.4 ml) and DCC ($SV_{T,\ DCC}$= 19.7 ml). Likewise, the increase in SV with the higher preload in DCC via the Frank-Starling mechanism is also evidenced in the graphs.

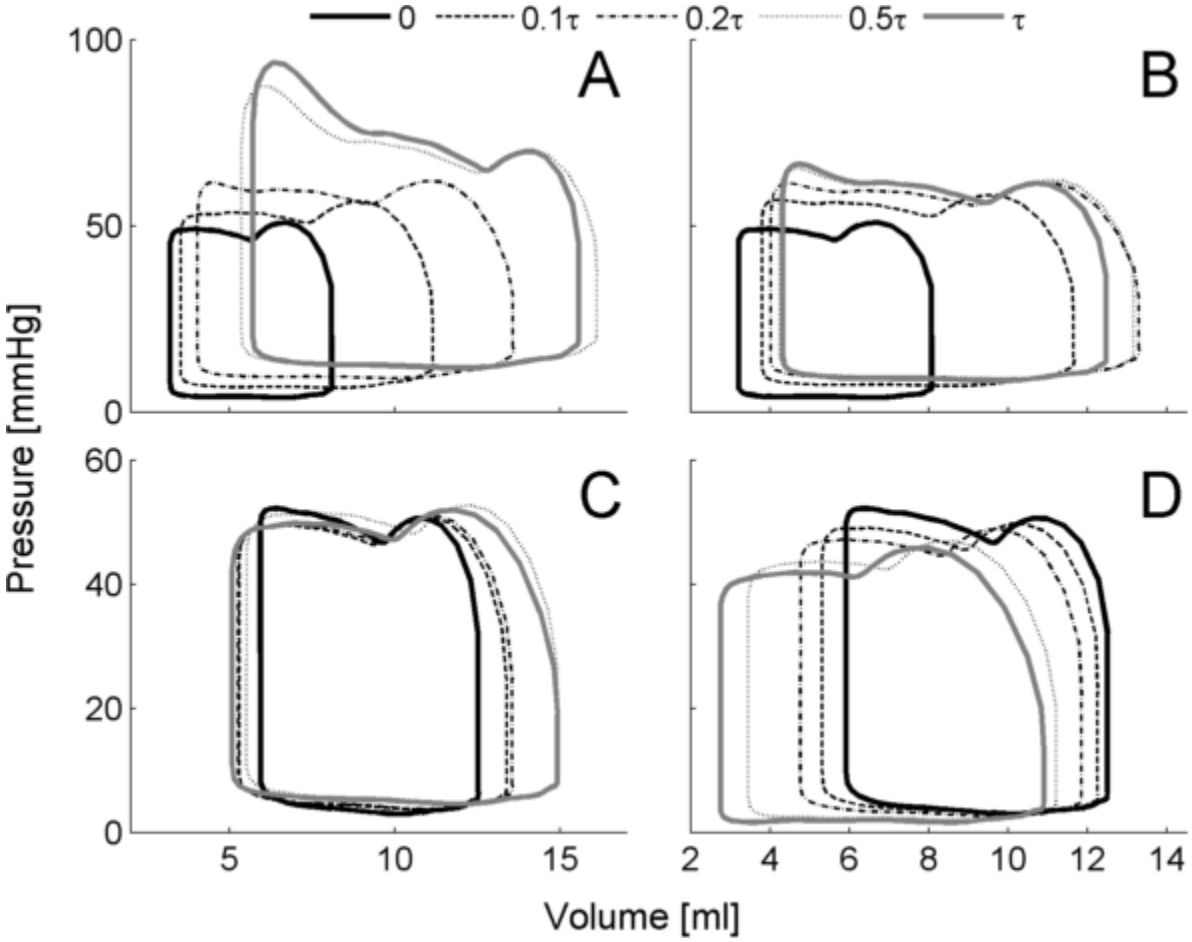

Figure 6.6 Pressure-volume (PV) loops sampled for one cardiac cycle at different time points during the transition. Legend shows the time point for each sample. A: PV curve sampled at LV in DCC. B: PV curve sampled at LV in ICC. C: PV curve sampled at RV in DCC. D: PV curve sampled at RV in ICC. Complete transition of all vessels were defined to complete at time = τ, which is 10 minutes in our simulation. Time is normalized to the τ. (LV: left ventricle, RV: right ventricle, DCC: delayed cord clamping, ICC: immediate cord clamping)

6.3.3 Gas Exchange and Oxygen Saturation during fetal transition

Figure 6.7 summarizes the impact of cord clamping on the oxygen saturation in the systemic aorta and the carotid arteries. Under the simulated conditions, ICC oxygen saturations were significantly lower than DCC, and encountered a 15-20% decrement in arterial oxygen saturations during the early transition. DCC provided a smoother transition in oxygen. At $t = 0.1\tau$, DCC and ICC carotid O_2 saturations were 55.7% and 33.8%, respectively. For DCC, 90% O_2 saturation was reached at 0.27τ through the transition, and with a delay of ~0.1 τ in the ICC case.

Our results agree well with the clinical observations with pulse oximetry, where peripheral arterial oxygen saturations (S_{pO2}) increase from 65% at 1 minutes after the cord clamped to 90% in 5 minutes of life [85, 86]. In a recent study [87], infants that are delivered with DCC and immediate skin-to-skin contact had a S_{pO2} of 80% at 1 minutes on the average, however reached full saturation slightly slower than the ICC infants.

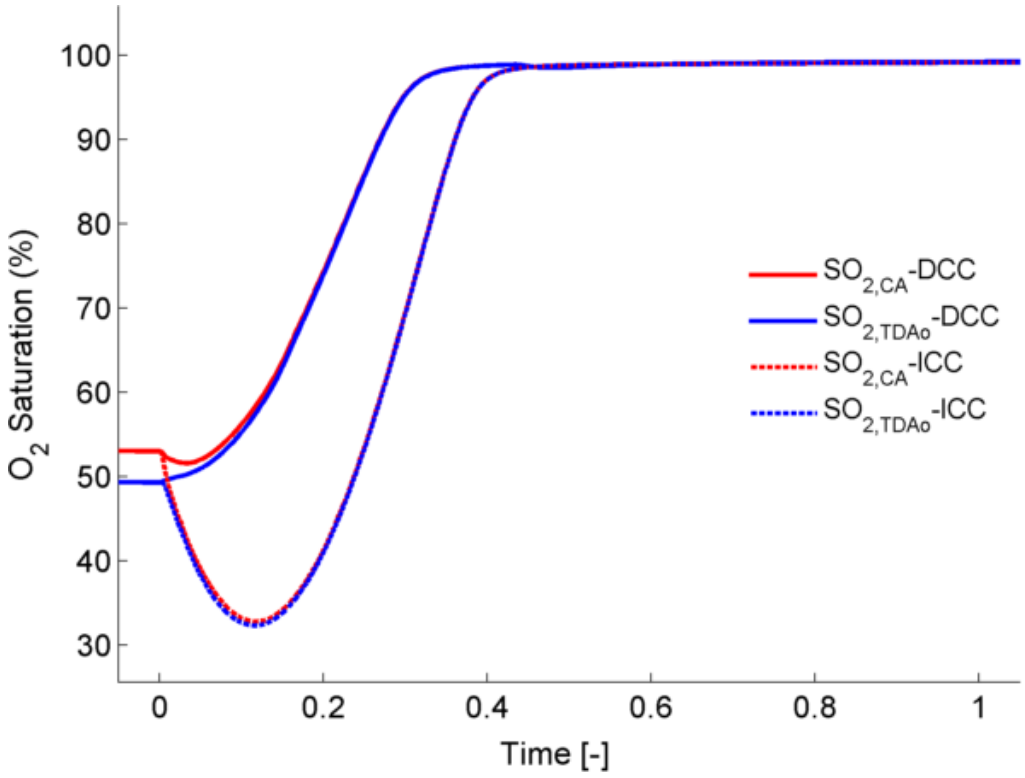

Figure 6.7 Oxygen saturation trends found to be different for DCC and ICC circulations. In ICC, a drop in the oxygen levels is observed before the lung ventilation stabilized. Depending on the duration of fetal transition this can be significant. O_2 saturations were sampled at the carotid arteries ($SO_{2,CA}$) and at the thoracic descending aorta ($SO_{2,TDAo}$). Complete transition of all vessels were defined to complete at time = τ, which is 10 minutes in our simulation. Time is normalized to the τ. (DCC: delayed cord clamping, ICC: immediate cord clamping)

6.4 Discussion

6.4.1 Placental transfusion improves ventricular function and hemodynamic stability

An important component of our model, which was not resolved by the previous animal or human studies, is the role of placental transfusion. Present simulations emphasized the significance of the additional placental blood volume introduced to the newborn circulation. In our model, placental transfusion increased the infant's blood volume by 19.3%, which resulted with a *persistent* increase in mean arterial (afterload) by 23.5% and in venous (preload) pressures by ~50% through the effect of the increased stressed blood volume (by 34%). In our simulation, placental transfusion volume (53.3ml) shows good agreement with clinical findings with clamping times of 60-120 seconds where measured blood volume increase were ~20% [52, 80, 81, 88].

The relation between afterload, preload, and ventricular diastolic stiffness/systolic contractility resulted with an increase in SV by 20.3%, therefore increasing the CO accordingly. This finding is supported by *in vivo* observations where CO and SVC flow was greater in DCC groups [71, 72]. In the instrumented preterm fetal lamb experiments [71], from the 5^{th} to 30^{th} minutes after the cord was clamped (end of the experiment), RVO was two folds greater for the group in which the cord was clamped 3.7 minutes after the ventilation was started, whereas the cord was clamped 2 minutes prior to the initiation of ventilation in the other group. In a clinical trial for preterm infants with 45 seconds DCC [72], SVC flow was 22-48% greater and RV SV was 8-40% greater between 6 to 108 hours after delivery. Neither of the studies reported the amount of placental transfusion volume. We should remark that the *in vivo* impact of placental transfusion on the CO can also be influenced by autoregulation and baroreflex effects such as

changes in peripheral resistance, venous tone, myocardial contractility, heart rate, and homeostatic mechanisms that may act to conserve the blood volume level, including transudation.

Comparative investigation of two umbilical cord clamping scenarios revealed that DCC yields smoother changes in the cardiac loads and hemodynamics during the transition. Delaying the cord clamping allowed the pulmonary flow to establish before a higher impedance load is imposed on the system with the removal of placental circulation, therefore preventing a rapid pressure increase in the arteries (Figure 6.5). ICC caused a pressure wave in the arteries that led to sudden increase in carotid blood pressure and cerebral blood flow. Such rapid alterations in arterial blood pressures and CO in the early transition caused by ICC may cause disturbances in the *in vivo* regulation and increase the risk of intraventricular hemorrhage. Similar hemodynamic stability issues in ICC that were accompanied with bradycardia were highlighted in Bhatt *et al.*'s study [71]. In this case, bradycardia is believed to be triggered by vagal stimulation in response to the pressure wave in the systemic arteries created by ICC [70, 89]. Due to the lack of baroreflex response in our model, we were unable to simulate bradycardia and the effects thereof.

6.4.2 Delayed cord clamping improves oxygenation at birth

We observed that DCC can significantly improve the oxygen saturation during the early transitional period when lungs are not yet fully active. In ICC, early clamping of the cord led to a significant drop in blood oxygen levels where carotid SO_2 dropped from 53% in fetus to 33.8% in under one minute (at 0.1τ in Figure 6.7). This may become more or less significant depending on the duration of transitional period and on the delay in the onset of respiration. In our findings, it is clear that placental respiration helps conserving arterial O_2 levels in case pulmonary respiration falls short. Likewise, this finding indicates that for clinical cases that require newborn

resuscitation, it could be the best practice to preserve the placental circulation in order to prevent severe hypoxia/asphyxia unless failure of placental function is the cause for the need of resuscitation. As stated by Niermeyer and Velaphi [70], conditions that may prevent delay in cord clamping include placental abruption, placenta previa, and tight nuchal cord; and some conditions will inevitably remain exclusion criteria for DCC, such as hemorrhage from vasa previa, velamentous cord insertion and cord avulsion.

The initial brief drop in arterial oxygen concentrations computed for ICC case in our simulations were not reported during the clinical measurements. A possible explanation can be attributed to the low resolution clinical recorders that may miss the rapid initial decline in O_2 saturations since pulse oximetry, the standard method to measure O_2 levels non-invasively immediately after birth [85, 86], can only be applied after the first minute in life. It is clearly observed from our model that DCC significantly helps the oxygenation of the newborn circulation. The clinical standard implies that the blood oxygen should reach complete saturation (>90%) during the first 10 minutes (median 7.9 minutes [86]). However, this standard is established mainly based on newborns who underwent ICC [85, 86, 90]. With DCC, it is possible to increase the rate at which oxygen reaches saturation [87]. Oxygen model calculations predicted that postnatal oxygen saturations to reach 90% requires less time with DCC than ICC.

6.4.3 Predictive capabilities and accuracy of the present model

Our modeling approach provided an accurate representation of the neonatal transition for human through the validation of fetal and neonatal circulation models, using clinical data for human and when absolutely necessary from lamb. *In silico* validation is primarily based on *in vivo* measurements of 1) central blood flow patterns during the fetal state (Figure 5.1 and Table 5.5)

[3, 45, 48], 2) organ level flow distribution (Figure 5.1 and Table 5.5) [3, 46], 3) dynamic changes in the CO [84, 91], arterial pressures [38, 49] and DA flow [76] during the transition (Figures 6.3-6.5). Although the birth related cardiovascular events have been investigated traditionally in the fetal lamb models [54, 71, 74-76], there are major differences between lamb and human cardiovascular systems, such as a higher blood flow distribution to the placenta in the term lamb fetus which is 40% CCO, compared to a 20% CCO in the human fetus at term [46]. Likewise, a lower pulmonary flow distribution, a larger fraction of umbilical venous return directed through the DV, and a significantly lower cerebral blood flow in the fetal lamb compared to human [3]. When using lamb data, for validation purposes, this comparative knowledge has been taken into account in the present LPM.

Table 6.4 Summary of the major hemodynamic events in the fetal to neonatal transition observed in the clinical practice and assessment of our model on its ability to capture them in its predictions.

Dynamic changes in cardiovascular function at birth	Prediction
Central flow patterns (DA, pulmonary) [76]	Captured
Temporal increase in LVO after birth [91]	Captured
Systemic and pulmonary blood pressure separation [38, 49]	Captured
Placental transfusion with DCC [92]	Captured
Long-term improvement of RVO and SVC flow with DCC [72]	Captured
Decreased CO immediately after birth with ICC [71]	Captured
Increased afterload immediately after birth with ICC [71]	Captured
Bradycardia in ICC [71]	Not captured
Higher SpO_2 in the early transition with DCC [87]	Captured

DA: ductus arteriosus, LVO: left ventricular output, RVO: right ventricular output, SpO_2: peripheral oxygen saturation, DCC: delayed cord clamping, ICC: immediate cord clamping

The time-varying resistance transition model employed in our simulations captured the essential cardiovascular events observed *in vivo* during and after birth. Simulated dynamics in DA and PBF (Figure 6.3), ventricular outputs (Figure 6.4), arterial pressures (Figure 6.5), effects of cord clamping on the hemodynamics and gas levels (Figures 6.3 to 6.7) successfully captured the

major trends in clinical observations. A summary of the predictive capabilities of our model is summarized in Table 6.4.

6.4.4 Ductus Arteriosus flow patterns and indications on shunt remodeling

In ICC, the instantaneous removal of the placental circulation caused systemic pressure to increase rapidly and surpass the pulmonary pressure in less time compared to DCC. This led to an earlier reversal of the flow across the DA (Figure 6.3). Oxygen concentration through the DA in relation to the timing and the magnitude of the shunt flow can alter the remodeling of the DA diameter. For precise timing, computed oxygen concentration can be linked to the DA constriction [60, 93, 94] where an earlier influx of oxygen rich blood from the left heart may cause premature reduction of the DA diameter. Most importantly, DCC would prevent this early flow reversal. Further, placental transfusion can help preventing premature constriction of DA since placental blood contains prostaglandins, which may work as vasodilators in the DA. However, it is unknown to which extent the prostaglandins in the placental circulation play a role in the transition with placental transfusion.

The presence of a continued placental oxygen supply at birth can play a major role in the expansion of pulmonary circulation due to the vasoactive properties of oxygen. After the closure of FO (that occurs in a short time after birth – data not shown), all the placental return is directed to the RV and lungs. As a result, the lung vessels will receive a greater portion of the oxygenated placental blood, which should lead to further vasodilatation or at least preventing vasoconstriction, which might occur with deoxygenated blood.

6.4.5 Effect of transition time

All transition times in the model (τ) were set to 10 minutes, which is considered typical for pulmonary circulation, but can be short for the ductal transition. Therefore, we also tested several different transition times for DA, pulmonary, and the placental circulation, and the effects of their relative shifts. This additional verification study showed that the predicted transitional trends were similar in all simulations (data not shown for brevity). However, there were slight changes in the timing of hemodynamic events. DA reversal occurred earlier with a faster UA closure in DCC. If the DA constriction was slowed, temporal overshoot in PBF and LVO during the patent DA became more significant.

6.4.6 Limitations

Although our model has been rigorously compared to the clinically measured data and agrees well with qualitative clinical studies and clinical expertise, the inherent limitations of this work are acknowledged. While the choice of the resistance transition model was guided by measured fetal-to-neonatal pressure and flow data, there were no direct references to verify the assumed shunt diameter trajectories. The biochemical responses at birth, detailed lung expansion and liquid clearance, metabolic adjustments, cardiopulmonary interactions, autoregulation and baroreflex response, as well as detailed systemic compartments have not been modeled, in order to achieve a simpler model with fewer variables. Inertance effects are similarly neglected due to lower Womersley number of fetal circulation. Incorporating these responses would no doubt improve the accuracy of the model's predictions, however the relative impact of placental transfusion-or-immediate cord clamping as illustrated here is not expected to change significantly.

6.4.7 Future utility of fetal transition LPM

In addition to healthy human newborn circulation, our LPM can also be applied to patients with congenital heart defects (CHD) having modified circuit topologies, where understanding and clinical management of the transition period is more critical. A variety of disease conditions or birth related complications can be simulated with small adjustments to the model. Such complications may arise from vascular structural malformations, placental, renal or respiratory diseases. Major CHD templates [2] include atrial/ventricular septal defects, obstructive lesions, valvular atresia, PVR related shunting and cardiac failure, persistent or congenital shunts, coarctation of the aorta, transposition of great arteries (TGA), hypoplastic left heart syndrome (HLHS), and Tetralogy of Fallot. These disease conditions were not investigated in the literature regarding the fetal transition and cord clamping . Prevalence of CHD is about 1% thus an optimal cord clamping strategy can be planned before birth and be beneficial as some of these are detected antenatally. For some CHD templates such as, obstructive lesions, HLHS, TGA, valvular atresia, survival is dependent on the postnatal patency of DA [2] if atrial or ventricular septal defects are not present. Therefore, early survival can be influenced positively or negatively depending on the disease specific cord-clamping scenario. For instance, patent ductus arteriosus (PDA) at birth is crucial for survival in TGA and HPLH patients, until a surgery can be carried out. Prostaglandins are given at birth to maintain a PDA [95], in this case DCC can help supplement prostaglandins. If the DA is closed rapidly at birth, placental circulation can be crucial as a source of resuscitation for TGA patients. Further, PDA and patent FO are not apparent until after birth and in theory could be influenced by the timing of cord clamping. Modeling of such conditions may result improved clinical management procedures for the transition to postnatal circulation and cord clamping. Likewise, such modeling examples can be integrated in the clinical training as an educational tool for neonatologists.

6.5 Conclusion

Quantitative knowledge of gestational hemodynamics is crucial in the management of neonatal care. We constructed a system-level LPM of the fetal-to-neonatal transition in human, which is validated rigorously with the existing *in vivo* clinical data. This model demonstrates that ICC can lead to an earlier onset of DA flow reversal and a reduced CO, meanwhile DCC imposes increased blood pressures due to an increased blood volume, and a higher CO through the Frank-Starling mechanism. For cases where the pulmonary ventilation is gradually established or delayed, ICC caused critically low oxygen saturations at the thoracic descending aorta and the carotid arteries due to rapidly depleting oxygen stores, whereas DCC prevented the oxygen levels to drop below the critical threshold by continued placental respiration. Our findings contribute to the literature by showing the link between placental transfusion and increased cardiac performance in the term infant; and show that DCC is advantageous over ICC in a case of inadequate pulmonary ventilation, unless there is a placental disease or incompetency. For future work, this model can be adapted to special clinical cases including the patients requiring neonatal resuscitation as well as patients with congenital heart diseases.

Chapter 7

The impact of maternal hyperoxygenation therapy on steady and pulsatile flow dynamics in the aortic vessels of hypoplastic left heart syndrome fetus.

7.1 Introduction

Hypoplastic left heart syndrome is caused by the underdevelopment of the the left side of the heart including aorta, aortic valve, left ventricle and mitral valve. In HLHS, blood returning from the lungs must flow through an opening in the wall of the atria (atrial septal defect). The right ventricle pumps the blood into the pulmonary artery and blood reaches the aorta through a patent ductus arteriosus. Survival on the first days of life depends on the patency of ductus arteriosus. Until an operation is performed, the ductus is kept open by intravenous medication.

HLHS surgery is carried out in several stages (Figure 7.1). The first stage is called the Norwood procedure [96]. Norwood procedure allows the right ventricle to pump blood to both the lungs and the body without the need for the ductus to be kept open. The aorta is reconstructed to make it large enough to supply the systemic blood flow pumped by the single ventricle. For this purpose, main pulmonary artery is separated from the two pulmonary arteries and joined with the underdeveloped section of the aorta. Since pulmonary arteries are no longer connected to the right ventricle, blood is directed to the lungs through a Blalock-Taussig shunt (located between the pulmonary artery to the subclavian artery) or a Sano shunt (located between the single ventricle and the pulmonary artery). The first stage is performed soon after birth while the ductus arteriosus is still open. The second stage (bidirectional Glenn or hemi-Fontan) is generally performed between 4 and 12 months. In this stage superior vena cava is separated from the right atria and joined with the pulmonary artery. The third stage (lateral tunnel Fontan or extracardiac

Fontan) is performed between 18 months and 3 years. Lateral tunnel Fontan connects the inferior vena cava to the pulmonary arteries through a lateral shunt located in the right atria. In extracardiac Fontan, same configuration is achieved with an extracardiac shunt. After the third stage reconstruction, systemic and pulmonary circulations are connected in series. This allows the deoxygenated blood flowing from the upper and lower body to directly flow to the pulmonary arteries where the blood is oxygenated.

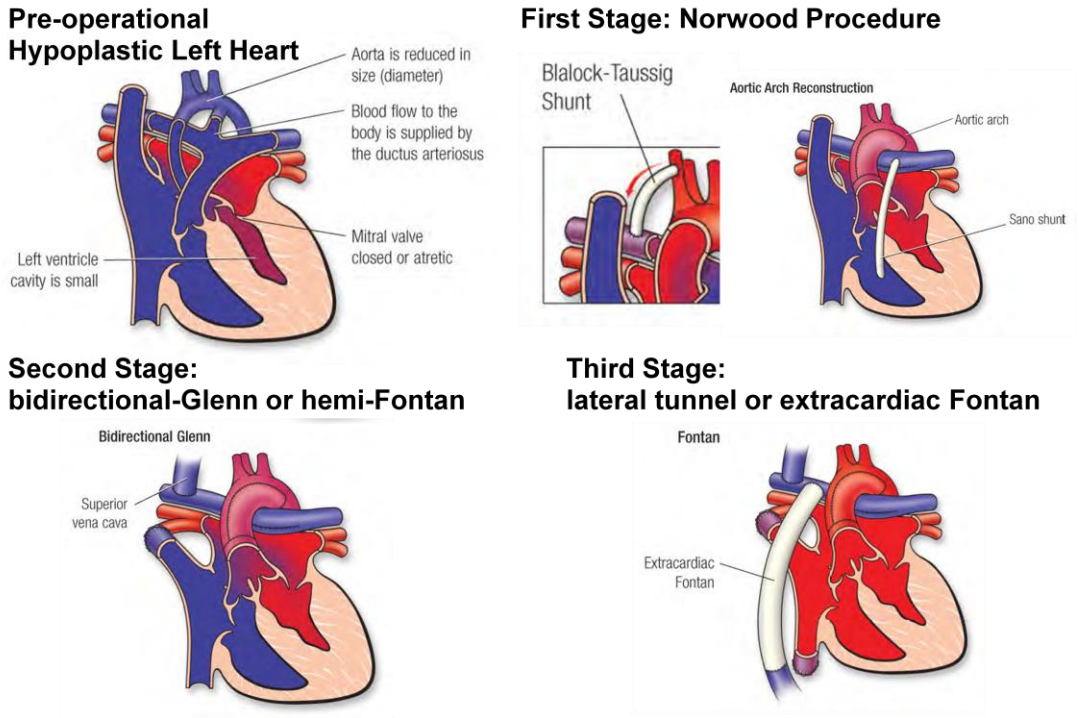

Figure 7.1 Hypoplastic left heart syndrome. In the pre-operational stage, left side of the heart is underdeveloped and systemic blood flow is supplied by ductus arteriosus. Norwood is the first stage of procedures where aorta is reconstructed. Pulmonary blood flow is supplied by the Blalock-Taussig shunt or the Sano shunt. Second stage of the surgeries is the bi-directional Glenn or hemi-Fontan. In this stage, superior vena cava is connected to the pulmonary artery. Third stage of the surgery is a lateral tunnel Fontan (intracardiac) or an extracardiac Fontan. After third stage reconstruction systemic and pulmonary circulations are connected in series. This prevents the mixing of oxygenated and deoxygenated bloods in the circulation.

The success of the aortic reconstruction during the Norwood procedure depends significantly on the pre-operative diameter of the aorta. A larger aorta facilitates the surgical procedure and lessens the requirement for additional vascular tissue during the reconstruction of

aorta. Vascular growth is influenced by the magnitude and pulsatility of the shear stress created by the blood flow. We hypothesize that it is possible to trigger aortic development in HLHS by maintaining a larger flow in the hypoplastic ascending aorta and the transverse aortic arch (aortic isthmus). Materno-fetal hyperoxygenation therapy was shown to increase the pulmonary venous return by the vasodilatory effect of oxygen on the pulmonary circulation [97]. It is also known that increased oxygen tension has a vasoconstrictor effect on the ductus arteriosus [3, 60]. Increased pulmonary return consequently increases the left ventricular filling and output. Through this effect, maternal hyperoxygenation therapy was used in the clinic to promote the development of hypoplastic but otherwise normal (normal or slightly abnormal morphologies) vessels at the left side of the heart (ascending aorta, aortic arch, aortic isthmus) [98-100].

In order to investigate the changes in flow metrics during the maternal hyperoxygenation, we developed a hypoplastic left heart LPM and conducted a parametric analysis on the impact of pulmonary vascular resistance and ductus arteriosus resistance on the left ventricular output and resulting pulsatile and steady flow metrics. In this study, we consider the underdeveloped left side of the heart, but valves are not atretic and the left ventricle is functional.

7.2 Methods

Fetal LPM that we developed in the previous chapters is used. In the HLHS circulation, left side of the heart is underdeveloped and the ductus arteriosus is enlarged due to a large right to left shunt [3]. Starting from the healthy fetus, we simulated the baseline HLHS condition by reducing the radius of LPM parameters of the left side (Mitral valve, left ventricle, aortic valve, ascending aorta, aortic arch and aortic isthmus) by half of its initial size, and increasing the ductus arteriosus diameter by twice of its initial size. For steady pipe flow, **E7.1** to **E7.3** gives the resistance (R),

compliance (*C*) and volume (*V*) with respect to the vessel length (*l*), inner radius (*r*), wall thickness (*h*), blood viscosity (μ) and elastic modulus of the vessel wall (*E*).

$$R = \frac{8\mu l}{\pi r^4} \quad \text{E7.1}$$

$$C = \frac{3\pi r^3 l}{2Eh} \quad \text{E7.2}$$

$$V = \pi r^2 l \; or = 4/3\pi r \quad \text{E7.3}$$

Assuming that considered vessel segments and the ventricle behave as tubes with steady flow, initial resistance (*R*), compliance (*C*) and volume (*V*) parameters are scaled according to E7.4 to E7.6 where subscript *i* represents the initial value at the healthy fetal conditions.

$$R = R_i(r/r_i)^{-4} \quad \text{E7.4}$$

$$C = C_i(r/r_i)^3 \quad \text{E7.5}$$

$$V = V_i(r/r_i)^2 \; or \; V_i(r/r_i)^3 \text{ (for ventricle)} \quad \text{E7.6}$$

Therefore in order to obtain the baseline HLHS circulation, left side resistances are multiplied by 16, compliances are divided by 8, and volumes are divided by 4 for aortic vessels and valves, and compliances are divided by 8 for the left ventricle. Meanwhile ductus arteriosus resistance is divided by 16 to model the increased diameter.

Atrial septal defect is modeled as a foramen ovale that allows regurgitation in the reverse direction (from left to right atrium), but with an increased resistance on the reverse direction compared to the right to left direction.

In the simulations, we used an older version of the LPM that was covered in the previous chapters. In this version, arterial compliances are linear (parameters are adopted from [16]) and the classical elastance function with fixed volume intercept [9, 23] (see Chapter 2) is used.

Aside from these changes, all other parameters are kept as in the healthy fetal LPM.

In order to study the possible impact range of maternal hyperoxygenation on the aortic blood flow, we perform a parametric analysis by varying the pulmonary vascular resistance between its initial value and 1/4 times of its initial value. Similarly, ductus arteriosus resistance is varied between its initial value and sixteen times of its initial value. Within this range, a number of possible combinations of pulmonary vascular resistance and ductus resistance are simulated. Mean flow rate changes in the ascending aorta, in the aortic isthmus and in the ductus arteriosus are calculated. Pulsatility index (PI) is calculated by (systolic maximum instantaneous flow rate-diastolic minimum instantaneous flow rate)/(mean flow rate) for the ascending aorta, aortic isthmus, and the ductus arteriosus.

7.3 Results

Table7.1 shows a comparison of the flow distribution in the healthy and HLHS fetal models. Combined cardiac output of the left and right ventricles is significantly lower in the HLHS fetus compared to the healthy fetus (1168 ml/min in HLHS compared to 1600 ml/min in healthy). There is a significant shift of cardiac output towards the right ventricle. As a result of the increased systemic arterial resistance, there is a marked decrease in the cerebral and superior vena cava (SVC) blood flow distribution. Systemic blood flow (upper+lower body) distribution is not affected, resulting in a shift of flow distribution towards the lower body. As a result of the poor performance of the left ventricle, left atrial pressure exceeds the right atrial pressure and a regurgitative flow across the foramen ovale (FO) is observed. Ductus arteriosus flow is a significant right to left shunt that fully feeds the lower body and partially feeds the upper body (brain and upper trunk). The flow in the aortic isthmus is markedly lower in the HLHS fetus

compared to the healthy fetus (-6 %CCO in the HLHS vs. 12%CCO in healthy fetus. Negative value signifies a right to left flow in the isthmus).

Table7.1 Distribution of blood flow as percent combined cardiac output (CCO) in the baseline Hypoplastic Left Heart Syndrome (HLHS) model and the healthy fetal model

Flow Distribution (%CCO)	HLHS baseline model	Fetal Model
LVO	**18**	**43**
RVO	**81**	**57**
Pulmonary	**23**	**22**
Placental	**24**	**22**
DA	**59**	**36**
FO	**-4**	**21**
Brain	**17**	**21**
Systemic Flow	**77**	**78**
SVC	**24**	**31**
IVC	**53**	**47**
CCO (ml/min)	**1168**	**1600**

Table 7.2 shows the arterial blood pressures in the baseline HLHS fetus and the healthy fetal circuit. Pressures are sampled at the ascending aorta and the main pulmonary artery (ASC and MPA in Figure 5.1, respectively). In the ASC, there is a reduction in mean and pulsatile blood pressures by ~25% in the HLHS. On the other hand, even though there is a reduction in the mean blood pressures in the MPA (by 13%), pulse pressure (systolic blood pressure minus diastolic pressure) is significantly higher (2.3 folds of the healthy pulse pressure) in the HLHS circulation.

Table7.2 Arterial blood pressures (Ascending Aorta and Main Pulmonary Artery) in the baseline Hypoplastic Left Heart Syndrome (HLHS) model and the healthy fetal model.

Pressures (mmHg)	Systolic	Diastolic	Mean
Ascending Aorta (Healthy)	**59**	**32**	**42**
Ascending Aorta (HLHS)	**41**	**22**	**30**
Main Pulmonary Artery (Healthy)	**44**	**32**	**44**
Main Pulmonary Artery (HLHS)	**55**	**27**	**38**

Figure 7.2 shows the impact of maternal hyperoxygenation therapy on the CCO. The increase in DA resistance is always reflected in a decrease in CCO, of which the impact is reduced with decreasing pulmonary vascular resistance (PVR).

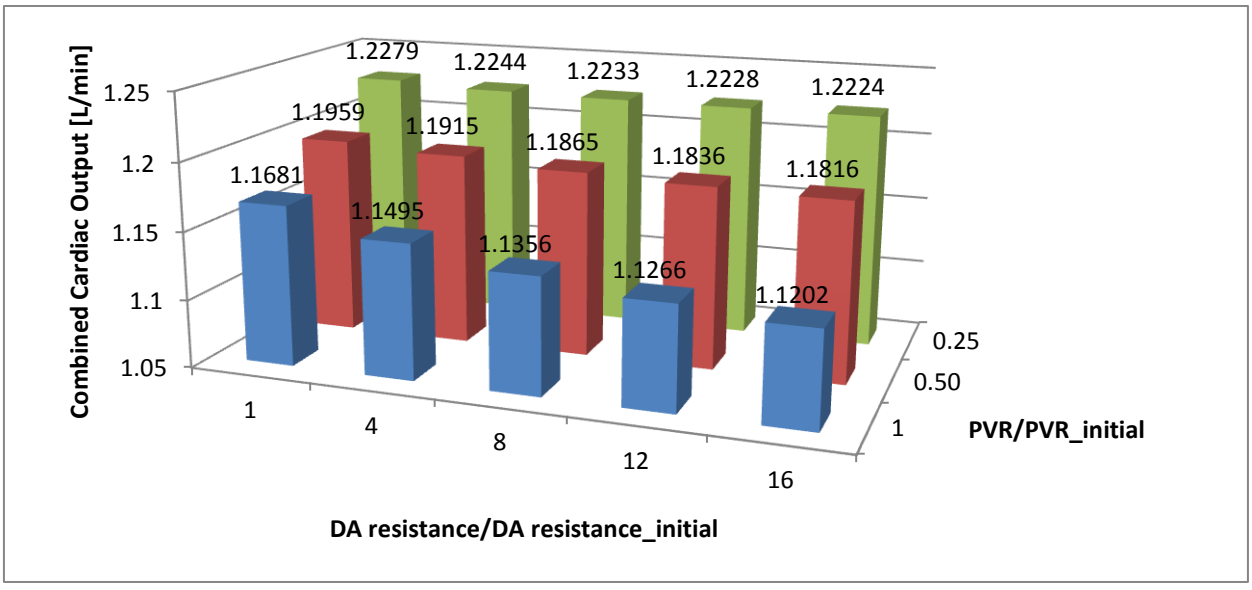

Figure 7.2 Impact of changes in ductus arteriosus resistance (DA) and pulmonary vascular resistance (PVR) on the combined cardiac output during the maternal hyperoxygenation therapy

Figure 7.3 shows the impact of maternal hyperoxygenation therapy on the average flow in the ascending aorta (ie. left ventricular output). The increase in DA resistance is always reflected

in an increase in the aortic flow rate. The same is valid for the decrease in PVR. A two-fold increase is possible when the DA resistance is at its highest and PVR is at its lowest.

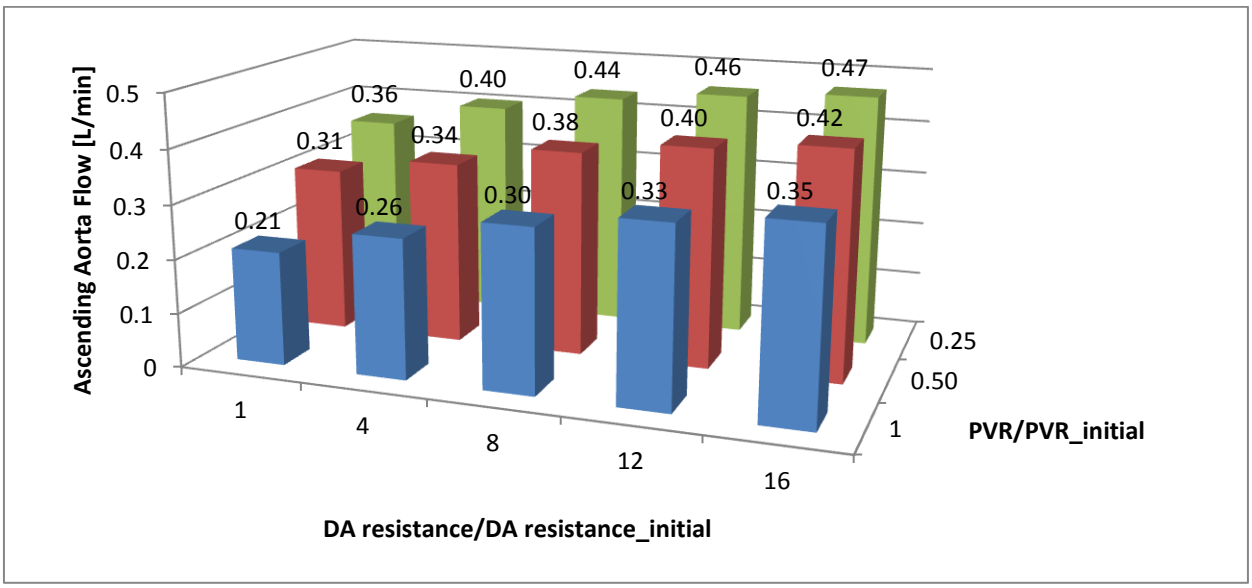

Figure 7.3 Impact of changes in ductus arteriosus resistance (DA) and pulmonary vascular resistance (PVR) on the mean ascending aorta flow rate during the maternal hyperoxygenation therapy

Figure 7.4 shows the impact of maternal hyperoxygenation therapy on the average flow in the aortic isthmus. A right to left (from the DA to the aortic arch) flow is observed in the baseline condition. The increase in DA resistance is always reflected in a shift in the direction of the isthmus flow from the right-to-left to left-to-right. The same is valid for the decrease in PVR. The average flow becomes zero along the red line displayed in Figure 7.3.3. A 1.7 fold increase in the magnitude of the isthmus flow rate (although the direction of flow is reversed) is possible when the DA resistance is at its highest and PVR is at its lowest.

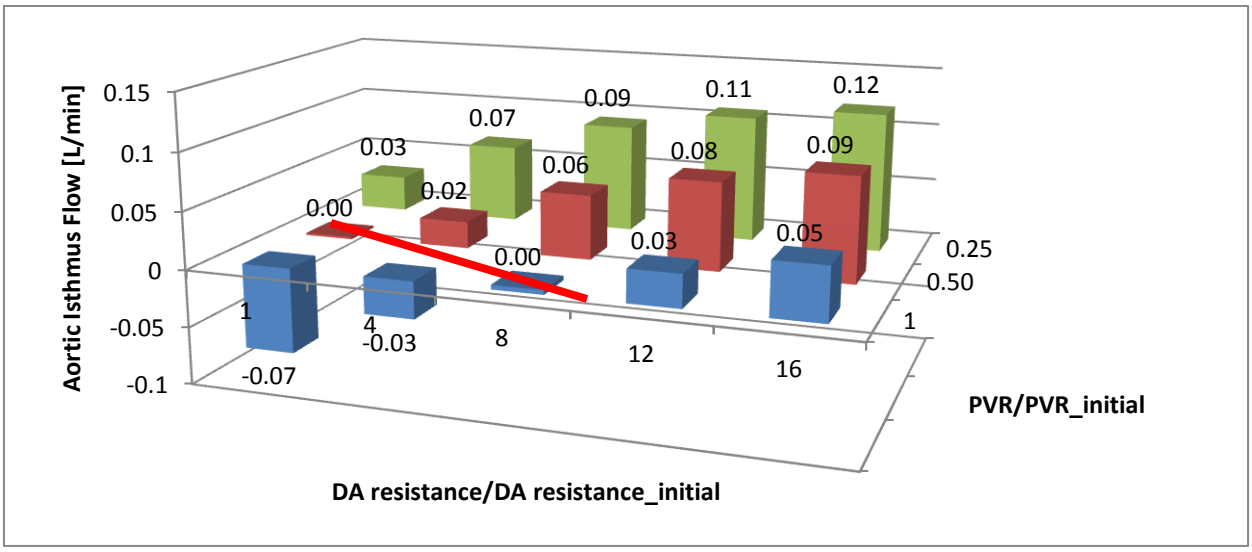

Figure 7.4 Impact of changes in ductus arteriosus resistance (DA) and pulmonary vascular resistance (PVR) on the aortic isthmus flow rate during the maternal hyperoxygenation therapy. Red line marks the region where average flow rate becomes zero (no net flow).

Figure 7.5 shows the impact of maternal hyperoxygenation therapy on the average flow in the ductus arteriosus (DA). A right to left (from the DA to the aortic arch) flow is observed in the baseline condition. The increase in DA resistance is always reflected in a decrease in the net right to left shunt. The same is valid for the decrease in PVR due to an increase in the left ventricular output.

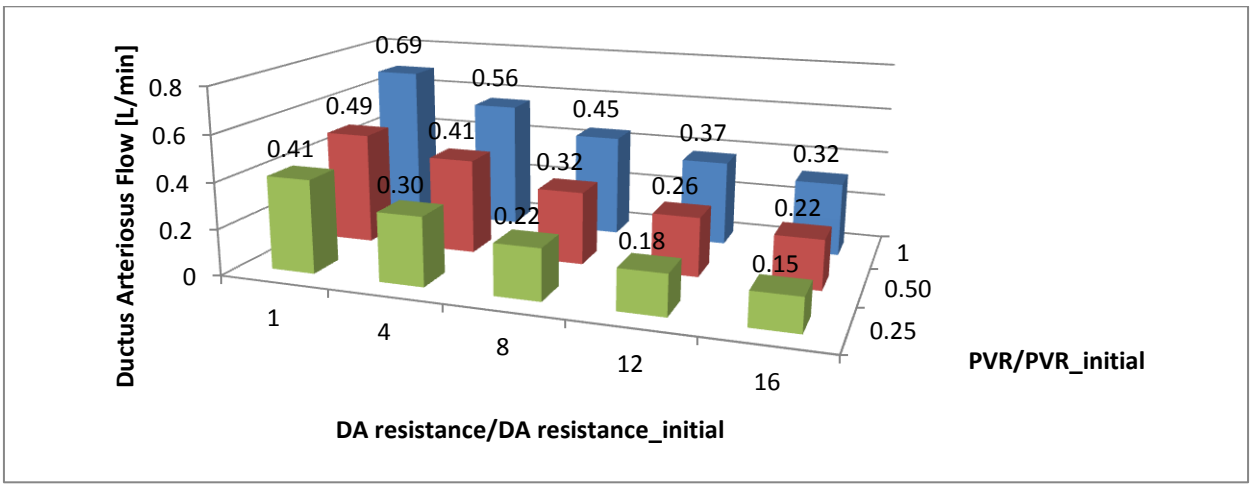

Figure 7.5 Impact of changes in ductus arteriosus resistance (DA) and pulmonary vascular resistance (PVR) on the net ductus arteriosus flow rate during the maternal hyperoxygenation therapy. Positive values indicate a right to left shunt.

Pulsatility index (PI) is unaffected in the ascending aorta with changes in the DA resistance and the PVR, having an almost consistent value of 2.36. This indicates that pulsatile flow difference changes similarly with the mean flow rate in the ASC.

Figure 7.6 shows the impact of maternal hyperoxygenation therapy on pulsatility index in the ductus arteriosus (DA). The increase in DA resistance is always reflected in a decrease in the PI_{DA}. The opposite is valid for the decrease in PVR, except for the case in which ductus resistance is at its initial value. In this case, PI_{DA} decreases with a reduction in the PVR by 50%, however with a further reduction to 25% PVR PI_{DA} increases above its baseline value.

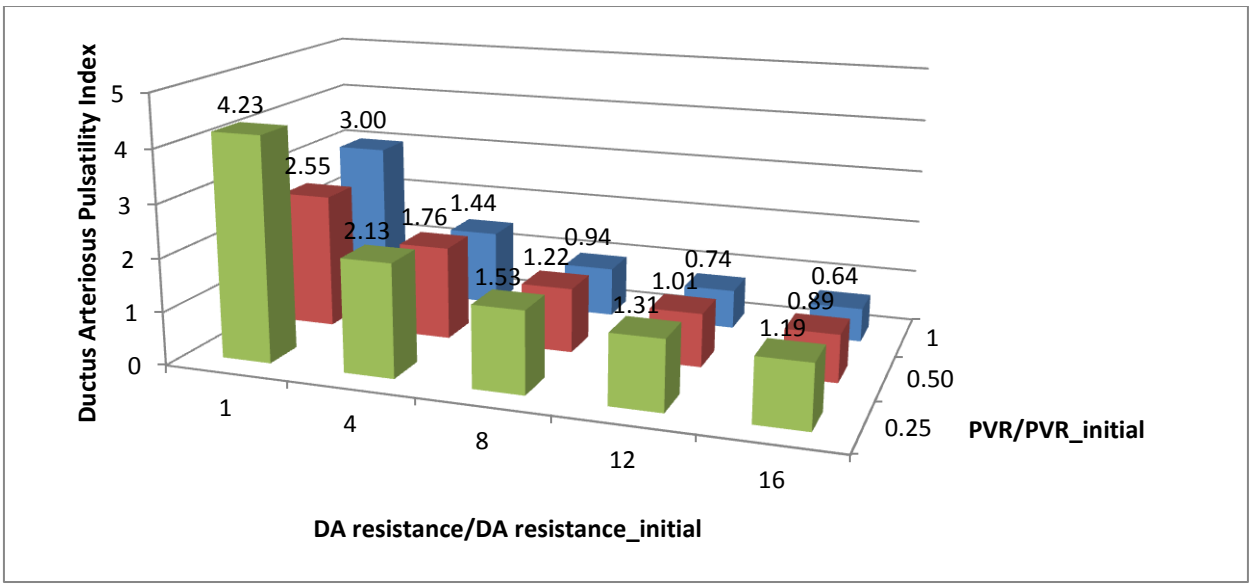

Figure 7.6 Impact of changes in ductus arteriosus resistance (DA) and pulmonary vascular resistance (PVR) on the ductus arteriosus pulsatility index during the maternal hyperoxygenation therapy.

7.4 Discussion

Fetal oxygenation has an established vasodilatory influence on the fetal pulmonary circulation, and increases in pulmonary flow was observed in the clinic [97]. Thus, maternal hyperoxygenation therapy was employed in the clinic to promote the growth of hypoplastic left

ventricle, ascending aorta, aortic arch, and aortic isthmus through an increased left ventricular output. It can be used to prevent the aortic coarctation due to low isthmus flow [98-100].

This parametric study investigates the possible impact of maternal hyperoxygenation related ductus and pulmonary remodeling on the flow dynamics in the aorta and ductus arteriosus. We showed that pulmonary vasodilatation and ductus vasoconstriction effectively improves both the mean and pulsatile flow in the ascending aorta and the left ventricle that can be as high as two times its initial value. Magnitude and direction of the aortic isthmus flow is determined by the interaction between the left and right ventricular outputs. At the baseline HLHS condition, blood pumped by the right ventricle is shunted through the ductus arteriosus and the aortic isthmus to the cerebral and upper body, thus called a right to left shunt. Vasoconstriction of the DA and vasodilatation of PVR results in a direction shift in the aortic isthmus flow towards left-to-right (meaning that left ventricular output supplies the cerebral flow fully and partially supplies the lower body flow through the isthmus). Regarding this finding, high oxygen pressures should be applied in order to effectively improve isthmus flow rates without causing stagnating flows. Findings also indicate that aortic pulsatile flow can be effectively improved with maternal hyperoxygenation. Combined cardiac output is affected to a lesser extent compared to other flow metrics.

7.5 Conclusion

Simulations indicate that maternal hyperoxygenation can be used to effectively improve mean and pulsatile flow metrics in the hypoplastic regions affected by HLHS.

Bibliography

1. Kiserud, T., *Physiology of the fetal circulation.* Semin Fetal Neonatal Med, 2005. **10**(6): p. 493-503.
2. Rudolph, A.M., *The changes in the circulation after birth. Their importance in congenital heart disease.* Circulation, 1970. **41**(2): p. 343-59.
3. Rudolph, A.M., *Congenital diseases of the heart : clinical-physiological considerations*. 3rd ed. 2009, Chichester, UK ; Hoboken, NJ: Wiley-Blackwell. 538 p.
4. Friedman, A.H. and J.T. Fahey, *The transition from fetal to neonatal circulation: normal responses and implications for infants with heart disease.* Semin Perinatol, 1993. **17**(2): p. 106-21.
5. Frank, O., *Die grundform des arteriellen pulses.* Z Biol, 1899. **37**(483-526): p. 19.
6. Westerhof, N., J.W. Lankhaar, and B.E. Westerhof, *The arterial Windkessel.* Med Biol Eng Comput, 2009. **47**(2): p. 131-41.
7. Stergiopulos, N., J.J. Meister, and N. Westerhof, *Determinants of stroke volume and systolic and diastolic aortic pressure.* Am J Physiol, 1996. **270**(6 Pt 2): p. H2050-9.
8. Segers, P., et al., *Systemic and pulmonary hemodynamics assessed with a lumped-parameter heart-arterial interaction model.* Journal of engineering mathematics, 2003. **47**(3-4): p. 185-199.
9. Suga, H., K. Sagawa, and A.A. Shoukas, *Load independence of the instantaneous pressure-volume ratio of the canine left ventricle and effects of epinephrine and heart rate on the ratio.* Circ Res, 1973. **32**(3): p. 314-22.
10. Stergiopulos, N., B.E. Westerhof, and N. Westerhof, *Total arterial inertance as the fourth element of the windkessel model.* American Journal of Physiology-Heart and Circulatory Physiology, 1999. **276**(1): p. H81-H88.
11. Li, J.K., T. Cui, and G.M. Drzewiecki, *A nonlinear model of the arterial system incorporating a pressure-dependent compliance.* IEEE Trans Biomed Eng, 1990. **37**(7): p. 673-8.
12. Shi, Y., P. Lawford, and R. Hose, *Review of zero-D and 1-D models of blood flow in the cardiovascular system.* Biomed Eng Online, 2011. **10**: p. 33.
13. Noordergraaf, A., P.D. Verdouw, and H.B. Boom, *The use of an analog computer in a circulation model.* Progress in cardiovascular diseases, 1963. **5**(5): p. 419-439.
14. Avolio, A., *Multi-branched model of the human arterial system.* Medical and Biological Engineering and Computing, 1980. **18**(6): p. 709-718.
15. Tu, C. and C.S. Peskin, *Hemodynamics in transposition of the great arteries with comparison to ventricular septal defect.* Comput Biol Med, 1989. **19**(2): p. 95-128.
16. Pennati, G., M. Bellotti, and R. Fumero, *Mathematical modelling of the human foetal cardiovascular system based on Doppler ultrasound data.* Med Eng Phys, 1997. **19**(4): p. 327-35.
17. Pennati, G. and R. Fumero, *Scaling approach to study the changes through the gestation of human fetal cardiac and circulatory behaviors.* Ann Biomed Eng, 2000. **28**(4): p. 442-52.
18. Sundareswaran, K.S., et al., *The total cavopulmonary connection resistance: a significant impact on single ventricle hemodynamics at rest and exercise.* Am J Physiol Heart Circ Physiol, 2008. **295**(6): p. H2427-35.
19. Pekkan, K., et al., *Coupling pediatric ventricle assist devices to the Fontan circulation: simulations with a lumped-parameter model.* ASAIO J, 2005. **51**(5): p. 618-28.
20. Vallecilla, C., et al., *Effect of high altitude exposure on the hemodynamics of the bidirectional Glenn physiology: Modeling incremented pulmonary vascular resistance and heart rate.* Journal of biomechanics, 2014. **47**(8): p. 1846-1852.
21. Phillips, C., R.L. Simon-Walker, and L.P. Dasi, *Energy Costs of Singular and Concomitant Pressure and Volume Overload Lesions.* Cardiovascular Engineering and Technology, 2014. **5**(1): p. 44-53.

22. Peskin, C.S. and C. Tu, *Hemodynamics in congenital heart disease.* Comput Biol Med, 1986. **16**(5): p. 331-59.
23. Hoppensteadt, F.C., C.S. Peskin, and F.C. Hoppensteadt, *Modeling and simulation in medicine and the life sciences*. 2nd ed. Texts in applied mathematics. 2002, New York: Springer. 5-108.
24. Huikeshoven, F.J., et al., *Mathematical model of fetal circulation and oxygen delivery.* Am J Physiol, 1985. **249**(2 Pt 2): p. R192-202.
25. Sá Couto, P.M., et al., *Mathematical model for educational simulation of the oxygen delivery to the fetus.* Control Engineering Practice, 2002. **10**(1): p. 59-66.
26. Bellotti, M., et al., *Dilatation of the ductus venosus in human fetuses: ultrasonographic evidence and mathematical modeling.* Am J Physiol, 1998. **275**(5 Pt 2): p. H1759-67.
27. Luria, O., et al., *Inverse solution of the fetal-circulation model based on ultrasound Doppler measurements.* Cardiovascular Engineering and Technology, 2014. **5**(2): p. 202-216.
28. Garcia-Canadilla, P., et al., *A Computational Model of the Fetal Circulation to Quantify Blood Redistribution in Intrauterine Growth Restriction.* PLoS computational biology, 2014. **10**(6): p. e1003667.
29. Sa-Couto, C.D., et al., *A model for educational simulation of hemodynamic transitions at birth.* Pediatr Res, 2010. **67**(2): p. 158-65.
30. Corsini, C., et al., *An integrated approach to patient-specific predictive modeling for single ventricle heart palliation.* Comput Methods Biomech Biomed Engin, 2013.
31. Suga, H. and K. Sagawa, *Instantaneous pressure-volume relationships and their ratio in the excised, supported canine left ventricle.* Circulation research, 1974. **35**(1): p. 117-126.
32. Claessens, T.E., et al., *Nonlinear isochrones in murine left ventricular pressure-volume loops: how well does the time-varying elastance concept hold?* Am J Physiol Heart Circ Physiol, 2006. **290**(4): p. H1474-83.
33. Georgakopoulos, D., et al., *In vivo murine left ventricular pressure-volume relations by miniaturized conductance micromanometry.* Am J Physiol, 1998. **274**(4 Pt 2): p. H1416-22.
34. Senzaki, H., C.H. Chen, and D.A. Kass, *Single-beat estimation of end-systolic pressure-volume relation in humans. A new method with the potential for noninvasive application.* Circulation, 1996. **94**(10): p. 2497-506.
35. Lankhaar, J.W., et al., *Modeling the instantaneous pressure-volume relation of the left ventricle: a comparison of six models.* Ann Biomed Eng, 2009. **37**(9): p. 1710-26.
36. Langewouters, G.J., K.H. Wesseling, and W.J. Goedhard, *The static elastic properties of 45 human thoracic and 20 abdominal aortas in vitro and the parameters of a new model.* J Biomech, 1984. **17**(6): p. 425-35.
37. Hamill, N., et al., *Fetal cardiac ventricular volume, cardiac output, and ejection fraction determined with 4-dimensional ultrasound using spatiotemporal image correlation and virtual organ computer-aided analysis.* Am J Obstet Gynecol, 2011. **205**(1): p. 76 e1-10.
38. Emmanouilides, G.C., et al., *Pulmonary Arterial Pressure Changes in Human Newborn Infants from Birth to 3 Days of Age.* J Pediatr, 1964. **65**: p. 327-33.
39. Shadwick, R.E., *Mechanical design in arteries.* J Exp Biol, 1999. **202**(Pt 23): p. 3305-13.
40. Steer, P.J., *Maternal hemoglobin concentration and birth weight.* Am J Clin Nutr, 2000. **71**(5 Suppl): p. 1285S-7S.
41. Hlastala, M.P. and A.J. Berger, *Physiology of respiration*. 2nd ed. 2001, Oxford ; New York: Oxford University Press. ix, 275 p.
42. Wang, Y. and S. Zhao, in *Vascular Biology of the Placenta*. 2010: San Rafael (CA).
43. Carter, A.M., *Placental oxygen consumption. Part I: in vivo studies--a review.* Placenta, 2000. **21 Suppl A**: p. S31-7.

44. Kiserud, T., S. Rasmussen, and S. Skulstad, *Blood flow and the degree of shunting through the ductus venosus in the human fetus.* Am J Obstet Gynecol, 2000. **182**(1 Pt 1): p. 147-53.
45. Mielke, G. and N. Benda, *Cardiac output and central distribution of blood flow in the human fetus.* Circulation, 2001. **103**(12): p. 1662-8.
46. Kiserud, T., et al., *Fetal cardiac output, distribution to the placenta and impact of placental compromise.* Ultrasound Obstet Gynecol, 2006. **28**(2): p. 126-36.
47. Molina, F.S., et al., *Heart stroke volume and cardiac output by four-dimensional ultrasound in normal fetuses.* Ultrasound Obstet Gynecol, 2008. **32**(2): p. 181-7.
48. Rasanen, J., et al., *Role of the pulmonary circulation in the distribution of human fetal cardiac output during the second half of pregnancy.* Circulation, 1996. **94**(5): p. 1068-73.
49. Kitterman, J.A., R.H. Phibbs, and W.H. Tooley, *Aortic blood pressure in normal newborn infants during the first 12 hours of life.* Pediatrics, 1969. **44**(6): p. 959-68.
50. Liu, Z., K.P. Brin, and F.C. Yin, *Estimation of total arterial compliance: an improved method and evaluation of current methods.* Am J Physiol, 1986. **251**(3 Pt 2): p. H588-600.
51. Yin, F.C. and C.T. Ting, *Compliance changes in physiological and pathological states.* J Hypertens Suppl, 1992. **10**(6): p. S31-3.
52. Usher, R., M. Shephard, and J. Lind, *The Blood Volume of the Newborn Infant and Placental Transfusion.* Acta Paediatr, 1963. **52**: p. 497-512.
53. Ville, Y., et al., *Umbilical venous pressure in normal, growth-retarded, and anemic fetuses.* Am J Obstet Gynecol, 1994. **170**(2): p. 487-94.
54. Iwamoto, H.S., D. Teitel, and A.M. Rudolph, *Effects of birth-related events on blood flow distribution.* Pediatr Res, 1987. **22**(6): p. 634-40.
55. Anderson, D.F., et al., *Central shunt flows and pressures in the mature fetal lamb.* Am J Physiol, 1981. **241**(1): p. H60-H66.
56. Kowalski, W., O. Dur, and K. Pekkan, *Lumped Parameter Model for the Measurement of O2 and CO2 Concentration in Congenital Heart Defects*, in *BMES Annual Fall Meeting*. 2010: Austin, TX.
57. Lackman, F., et al., *Fetal umbilical cord oxygen values and birth to placental weight ratio in relation to size at birth.* Am J Obstet Gynecol, 2001. **185**(3): p. 674-82.
58. Sansoucie, D.A. and T.A. Cavaliere, *Transition from fetal to extrauterine circulation.* Neonatal Netw, 1997. **16**(2): p. 5-12.
59. McGrath, J.C., et al., *Contraction of human umbilical artery, but not vein, by oxygen.* J Physiol, 1986. **380**: p. 513-9.
60. Oberhansli-Weiss, I., et al., *The pattern and mechanisms of response to oxygen by the ductus arteriosus and umbilical artery.* Pediatr Res, 1972. **6**(9): p. 693-700.
61. Gray, H., et al., *Gray's anatomy : the anatomical basis of clinical practice*. 39th ed. 2005, Edinburgh ; New York: Elsevier Churchill Livingstone. 1052-4.
62. Raju, T.N., *Timing of umbilical cord clamping after birth for optimizing placental transfusion.* Curr Opin Pediatr, 2013. **25**(2): p. 180-7.
63. Hutchon, D.J., *EARLY VS DELAYED CORD CLAMPING AT BIRTH; IN SICKNESS AND IN HEALTH.* Fetal and Maternal Medicine Review, 2013.
64. Aladangady, N., et al., *Infants' blood volume in a controlled trial of placental transfusion at preterm delivery.* Pediatrics, 2006. **117**(1): p. 93-8.
65. van Rheenen, P.F. and B.J. Brabin, *A practical approach to timing cord clamping in resource poor settings.* BMJ, 2006. **333**(7575): p. 954-8.
66. Hutchon, D.J., *Delayed cord clamping may also be beneficial in rich settings.* BMJ, 2006. **333**(7577): p. 1073.
67. McDonald, S.J., et al., *Effect of timing of umbilical cord clamping of term infants on maternal and neonatal outcomes.* Cochrane Database Syst Rev, 2013. **7**: p. CD004074.

68. Chaparro, C.M., et al., *Effect of timing of umbilical cord clamping on iron status in Mexican infants: a randomised controlled trial.* Lancet, 2006. **367**(9527): p. 1997-2004.
69. Committee on Obstetric Practice, A.C.o.O. and Gynecologists, *Committee Opinion No.543: Timing of umbilical cord clamping after birth.* Obstet Gynecol, 2012. **120**(6): p. 1522-6.
70. Niermeyer, S. and S. Velaphi, *Promoting physiologic transition at birth: Re-examining resuscitation and the timing of cord clamping.* Semin Fetal Neonatal Med, 2013. **18**(6): p. 385-92.
71. Bhatt, S., et al., *Delaying cord clamping until ventilation onset improves cardiovascular function at birth in preterm lambs.* J Physiol, 2013. **591**(Pt 8): p. 2113-26.
72. Sommers, R., et al., *Hemodynamic effects of delayed cord clamping in premature infants.* Pediatrics, 2012. **129**(3): p. e667-72.
73. Rudolph, A.M., *Distribution and regulation of blood flow in the fetal and neonatal lamb.* Circ Res, 1985. **57**(6): p. 811-21.
74. Teitel, D.F., H.S. Iwamoto, and A.M. Rudolph, *Effects of birth-related events on central blood flow patterns.* Pediatr Res, 1987. **22**(5): p. 557-66.
75. Teitel, D.F., H.S. Iwamoto, and A.M. Rudolph, *Changes in the pulmonary circulation during birth-related events.* Pediatr Res, 1990. **27**(4 Pt 1): p. 372-8.
76. Crossley, K.J., et al., *Dynamic changes in the direction of blood flow through the ductus arteriosus at birth.* J Physiol, 2009. **587**(Pt 19): p. 4695-704.
77. Coceani, F. and P.M. Olley, *The response of the ductus arteriosus to prostaglandins.* Can J Physiol Pharmacol, 1973. **51**(3): p. 220-5.
78. Heymann, M.A., *Control of the pulmonary circulation in the fetus and during the transitional period to air breathing.* Eur J Obstet Gynecol Reprod Biol, 1999. **84**(2): p. 127-32.
79. Migliavacca, F., et al., *Computational model of the fluid dynamics in systemic-to-pulmonary shunts.* J Biomech, 2000. **33**(5): p. 549-57.
80. Vain, N.E., et al., *Effect of gravity on volume of placental transfusion: a multicentre, randomised, non-inferiority trial.* Lancet, 2014.
81. Yao, A.C., M. Hirvensalo, and J. Lind, *Placental transfusion-rate and uterine contraction.* Lancet, 1968. **1**(7539): p. 380-3.
82. Koch, G., *Alveolar ventilation, diffusing capacity and the A-a PO2 difference in the newborn infant.* Respir Physiol, 1968. **4**(2): p. 168-92.
83. Rothe, C.F., *Mean circulatory filling pressure: its meaning and measurement.* J Appl Physiol (1985), 1993. **74**(2): p. 499-509.
84. Agata, Y., et al., *Changes in left ventricular output from fetal to early neonatal life.* J Pediatr, 1991. **119**(3): p. 441-5.
85. Saugstad, O.D., *Oxygen saturations immediately after birth.* J Pediatr, 2006. **148**(5): p. 569-70.
86. Dawson, J.A., et al., *Defining the reference range for oxygen saturation for infants after birth.* Pediatrics, 2010. **125**(6): p. e1340-7.
87. Smit, M., et al., *Pulse oximetry in newborns with delayed cord clamping and immediate skin-to-skin contact.* Arch Dis Child Fetal Neonatal Ed, 2014.
88. Yao, A., M. Moinian, and J. Lind, *Distribution of blood between infant and placenta after birth.* The Lancet, 1969. **294**(7626): p. 871-873.
89. Brady, J.P. and L.S. James, *Heart rate changes in the fetus and newborn infant during labor, delivery, and the immediate neonatal period.* Am J Obstet Gynecol, 1962. **84**: p. 1-12.
90. Rabi, Y., et al., *Oxygen saturation trends immediately after birth.* J Pediatr, 2006. **148**(5): p. 590-4.
91. Agata, Y., et al., *Regional blood flow distribution and left ventricular output during early neonatal life: a quantitative ultrasonographic assessment.* Pediatr Res, 1994. **36**(6): p. 805-10.
92. Yao, A.C. and J. Lind, *Placental transfusion.* Am J Dis Child, 1974. **127**(1): p. 128-41.

93. Nakanishi, T., et al., *Mechanisms of oxygen-induced contraction of ductus arteriosus isolated from the fetal rabbit.* Circ Res, 1993. **72**(6): p. 1218-28.
94. Heymann, M.A. and A.M. Rudolph, *Control of the ductus arteriosus.* Physiol Rev, 1975. **55**(1): p. 62-78.
95. Elliott, R.B., M.B. Starling, and J.M. Neutze, *Medical manipulation of the ductus arteriosus.* Lancet, 1975. **1**(7899): p. 140-2.
96. Norwood, W.I., P. Lang, and D.D. Hansen, *Physiologic repair of aortic atresia-hypoplastic left heart syndrome.* The New England journal of medicine, 1983. **308**(1): p. 23.
97. Rasanen, J., et al., *Reactivity of the human fetal pulmonary circulation to maternal hyperoxygenation increases during the second half of pregnancy a randomized study.* Circulation, 1998. **97**(3): p. 257-262.
98. Kohl, T., et al., *Maternal hyperoxygenation in late gestation promotes rapid increase of cardiac dimensions in fetuses with hypoplastic left hearts with intrinsically normal or slightly abnormal aortic and mitral valves.* Ultraschall in der Medizin-European Journal of Ultrasound, 2008. **29**(S 2): p. S2_OP7.
99. Kohl, T., *Letter by Kohl Regarding Article,"Current Status of Fetal Cardiac Intervention".* Circulation, 2010. **122**(18): p. e506-e506.
100. Kohl, T., *Effects of maternal–fetal hyperoxygenation on aortic arch flow in a late-gestation human fetus with closed oval foramen at risk for coarctation.* The Journal of thoracic and cardiovascular surgery, 2011. **142**(2): p. e67-e69.